Identifying the regional emergence of climate patterns in a simulation of stratospheric aerosol injection

Zachary M. Labe[1,2,*], Elizabeth A. Barnes[1], and James W. Hurrell[1]

[1] Department of Atmospheric Science, Colorado State University, Fort Collins, CO, USA

[2] Now at Princeton University/NOAA Geophysical Fluid Dynamics Laboratory, Princeton, NJ, USA

[*] Email: zachary.labe@noaa.gov

Abstract. Stratospheric aerosol injection is a proposed form of solar climate invention (SCI) that could potentially reduce the amount of future warming from externally-forced climate change. However, more research is needed, as there are significant uncertainties surrounding the possible impacts of SCI, including unforeseen effects on regional climate patterns. In this study, we consider a climate model simulation of the deployment of stratospheric aerosols to maintain the global mean surface temperature at 1.5°C above pre-industrial levels. Leveraging two different machine learning methods, we evaluate when the effects of SCI would be detectable at regional scales. Specifically, we train a logistic regression model to classify whether an annual mean map of near-surface temperature or total precipitation is from a future climate under the influence of SCI or not. We then design an artificial neural network to predict how many years it has been since the deployment of SCI by inputting the regional maps from the climate intervention scenario. In both detection methods, we use feature attribution methods to spatially understand the forced climate patterns that are important for the machine learning model predictions. The effect of SCI on regional temperature patterns is detectable in under a decade for most regions. However, the effect of SCI on regional precipitation patterns is more difficult to distinguish due to the presence of internal climate variability.

Keywords: climate intervention, climate change, climate variability, machine learning, climate models, regional climate, large ensembles

Submitted to: *Environ. Res. Lett.*

This EarthArXiv original preprint has been submitted to Environmental Research Letters (ERL) and has not been peer-reviewed or edited.

1. Introduction

All components of the Earth system are experiencing rapid change due to human-driven activities, such as the emission of greenhouse gases (IPCC et al., 2021). In fact, the primary global mean surface temperature (GMST) monitoring datasets all agree that the last seven years (2015-2021) are the seven warmest on record (Dunn et al., 2021). The GMST is now consistently more than 1.1°C above the 1850-1900 pre-industrial reference period and therefore quickly approaching critical warming levels of 1.5°C and 2°C for even more consequential global climate change impacts (IPCC, 2018; McKay et al., 2022). The effects of human activities (i.e., the forced response) have already been detected outside the range of internal climate variability (Sippel et al., 2021), such as through changes to the regional hydrological cycle (e.g. Marvel et al., 2019; Madakumbura et al., 2021), modulation of the seasonality of tropospheric temperatures (Santer et al., 2022), cooling and contraction of the stratosphere (Pisoft et al., 2021), increases in some extreme weather events (e.g. Clarke et al., 2022), rising global sea levels and deep ocean heat content (e.g., Hsu and Velicogna, 2017; Cheng et al., 2022), and through the loss of ice mass in the global cryosphere (Slater et al., 2021).

Given the continued high levels of global carbon emissions (Liu et al., 2022), it is still uncertain whether countries' long-term pledges and commitments for net-zero emissions are enough to prevent overshooting Paris agreement targets within the next few decades (e.g., UNFCCC, 2015; Dvorak et al., 2022; Matthews and Wynes, 2022; Meinshausen et al., 2022). In addition to exploring technologies for a net-zero energy system (Davis et al., 2018), large-scale carbon capture and storage (de Kleijne et al., 2022), and other mitigation strategies, the deployment of solar climate intervention (SCI) technology has been discussed as a possible alternative for reducing the most adverse impacts of climate change (Kravitz and MacMartin, 2020). However, there are numerous ethical and political concerns, issues of feasibility, uncertainties in the Earth system response, and the potential for unforeseen consequences surrounding the use of SCI methods (Burns et al., 2016; Irvine et al., 2016; Carlson and Trisos, 2018; Mahajan et al., 2019; Abatayo et al., 2020). To better constrain the costs, risks, and benefits of SCI strategies, the National Academies of Science, Engineering and Medicine (NASEM) outlined a series of recommendations for conducting and supporting more research on this topic, including the impacts of SCI on regional patterns and extremes relative to climate change and natural variability (NASEM, 2021).

One often studied common form of SCI is through the potential deployment of stratospheric aerosols, otherwise known as stratospheric aerosol injection (Robock et al., 2008). By deliberately releasing sulfates, calcium carbonate, or other materials into the atmosphere, a small amount of incoming sunlight would be reflected back into space. Thus, this mechanism would act to cool Earth's climate in a manner that is analogous to the climate effects of an explosive volcanic eruption (Robock, 2000). Although coordinated modeling efforts, such as through the Geoengineering Model Intercomparison Project (GeoMIP) (Kravitz et al., 2011; Kravitz et al., 2015), have attempted to simulate the range of climate impacts from SCI, these attempts have made some unrealistic simplifications to future scenario choices and rarely considered the role of internal climate variability (MacMartin et al., 2022; Richter et al., 2022; Visioni and Robock, 2022).

The first large modeling ensemble to attempt to simulate SCI was the National Center for Atmospheric Research (NCAR) 20-member Geoengineering Large Ensemble (GLENS; Tilmes et al., 2018) performed with version 1 of the Community Earth System Model (CESM1; Hurrell et al., 2013) and using the Whole Atmosphere Community Climate Model version 4 (WACCM4; Mills et al., 2017). GLENS was simulated with several design simplifications in its implementation of SCI and considered an extreme future greenhouse gas emissions scenario (Representative Concentration Pathway; RCP8.5) (Richter et al., 2022). Barnes et al. (2022) recently examined the emergence of SCI impacts on climate extremes in GLENS and found that a simple machine learning method could detect whether a global map of extreme precipitation or extreme temperature came from a world under the influence of SCI or RCP8.5 alone in less than two decades. However, the magnitude of the forced climate responses within GLENS may be unrealistic due to the excessive amount of aerosols needed by the end of the 21st century to offset warming under RCP8.5 (Burgess et al., 2020; Peters and Hausfather, 2020). Thus, the regional detectability of SCI in a lower emissions scenario remains unexplored.

To address this question, an experiment called the Assessing Responses and Impacts of SCI on the Earth system with SAI (ARISE-SAI-1.5; Richter et al., 2022) has recently been conducted using a lower future emissions scenario (Shared Socioeconomic Pathway; SSP2-4.5). In this study, we address the question of the detectability and emergence of climate signals in ARISE-SAI-1.5 by extending the framework of Barnes et al. (2022) through several different ways. First, we design two separate machine learning methods to consider whether we can detect SCI impacts on regional climate, and if so, how long has it been since the initial aerosol injection. Second, we focus our analysis on different geographic locations, which range from global land areas to much smaller key climate regions, such as the Amazon basin. The advantage of using this data-driven approach is that we can identify time-evolving spatial patterns of forced climate signals due to SCI using explainable machine learning methods, rather than only quantify point-by-point summary statistics.

2. Data

We focus our analysis on the ARISE-SAI-1.5 experiment, which is a new SCI simulation conducted using NCAR's CESM2 (Danabasoglu et al., 2020) and its high-top atmospheric model component WACCM6 (Gettelman et al., 2019). This climate model is further described in text S1. While the specific design details of ARISE-SAI-1.5 are documented within Richter et al. (2022), we briefly summarize its implementation here. Two sets of 10-member ensembles each were performed using CESM2(WACCM6) to compare the effect of SCI. First, a control simulation was conducted using the SSP2-4.5 scenario (O'Neill et al., 2016), which is a medium future greenhouse gas emissions pathway that is in better agreement with recent cumulative emission trends (Hausfather and Peters, 2020). This simulation, which we refer to as "SSP2-4.5" in our analysis, covers 2015 to 2069.

We compare the SSP2-4.5 simulation with a SCI perturbation experiment, which we refer to as "SAI" in the results section. Similar to the control run, the SAI simulation uses the SSP2-4.5 future emissions scenario for each ensemble member, but begins climate intervention in the year 2035 by injecting stratospheric aerosols to maintain the GMST anomaly to 1.5°C above pre-industrial levels. In addition to limiting the GMST from rising, the controller for the aerosol injection also monitors and maintains the meridional temperature gradient and equator-to-pole temperature (MacMartin et al., 2014; Kravitz et al., 2017). As shown in figure 1 of Richter et al. (2022), the majority of the sulfur dioxide is injected at 15°S latitude and 21 km altitude.

For both simulations (SSP2-4.5 and SAI), we calculate annual means using gridded monthly CESM2(WACCM6) output. We focus our analysis over land areas using two common climate variables: near-surface air temperature (TREFHT; figure S1(a)) and total precipitation (PRECT; figure S1(b)).

3. Methods

To evaluate the detectability of SCI over different spatial regions, we first compare our machine learning results for global maps of temperature and precipitation. We then consider the Northern Hemisphere (0°N-90°N and 180°W-180°E) and the Southern Hemisphere (90°S-0°S and 180°W-180°E), along with six smaller geographic regions. These regions are outlined in figure S1 and include the Arctic, Antarctic, Tropics, Southeast Asia, Central Africa, and Amazon. They cover a wide range in climatological mean states and patterns of interannual variability, as shown for the latter portion of the SAI simulations in figures S1 and S2. Finally, in addition to evaluating climate signals over the entire 2035 to 2069 time series, we also compare two shorter periods - 2035 to 2044 and 2045 to 2069 - in order to account for at least 10 years of transition to a quasi-equilibrium state after the initial injection of stratospheric aerosols (Richter et al., 2022).

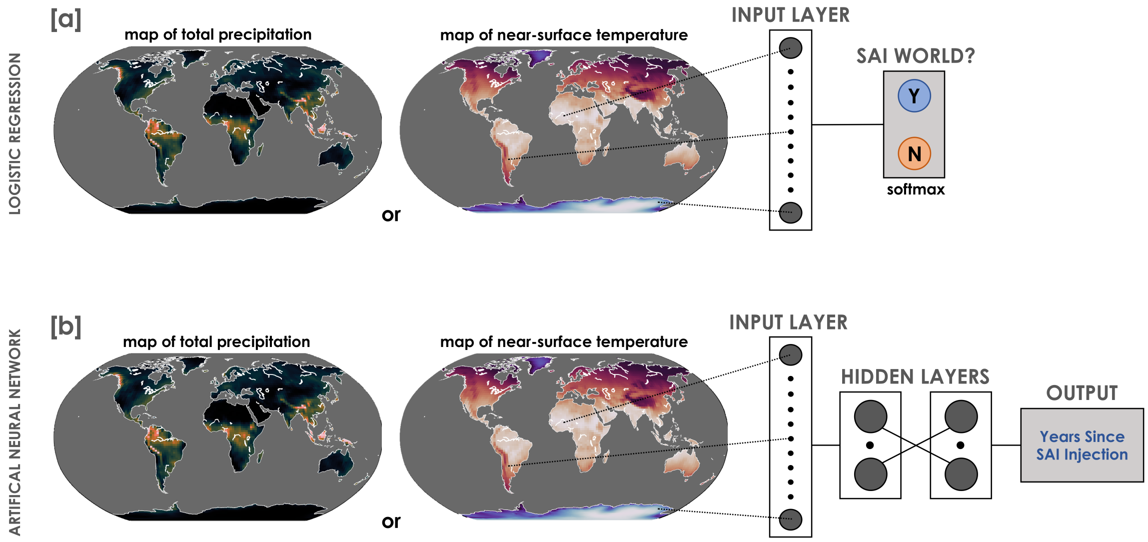

Figure 1. (a) Schematic of the logistic regression model used for classifying whether an annual mean map of near-surface temperature (TREFHT) or total precipitation (PRECT) is from the SAI scenario or SSP2-4.5 scenario. The logistic regression consists of a single linear layer and a softmax activation function in the output with two nodes (binary classification). (b) Schematic of the regression artificial neural network (ANN) architecture used to predict how many years it has been since the deployment of SAI in ARISE-SAI-1.5. The ANN consists of two hidden layers with 10 nodes each.

3.1. Logistic Regression

To first evaluate the timing of the emergence of SCI detectability for impacts on regional climate, we apply a logistic regression model to predict whether an annual mean map of temperature or precipitation is produced from either the SSP2-4.5 or SAI simulation (figure 1(a)). In other words, this is a binary classification problem. Our logistic regression model architecture (sometimes referred to as softmax regression) is comprised of an input layer and an output layer with two class nodes (i.e., SSP2-4.5 or SAI). A softmax activation function is applied to the output layer, which transforms the values into class probabilities that sum to one. This probability is referred to as the logistic regression model confidence. As an example, for the global regional analysis, our logistic regression model receives an input vector comprised of 13824 units, which are flattened maps of 96 latitude by 144 longitude points. The output layer then returns the confidence that this map was from the SAI or SSP2-4.5 climate model simulation. The class that is ultimately predicted is defined by a confidence value greater than 0.5.

For both SSP2-4.5 and SAI, we train on seven ensemble members (70% of the dataset), validate on two ensemble members, and test on one ensemble member. Note that the sensitivity of the results to different random initialization seeds and combinations of training ensemble members is explored within the supplementary data section (figures S3 and S4). More details on the logistic regression architecture can be found in text S2.

3.2. Artificial Neural Network

Next, we use an artificial neural network (ANN) to address a potentially more difficult prediction task. For this problem, we take maps of annual mean temperature and precipitation from the SAI simulation and train an ANN to predict how many years it has been since SCI was initiated (i.e., the year 2035) (figure 1(b)). To put in another way, we ask the question under the assumption that if the influence of SCI is indeed detectable, can we then determine when it first started? While there is no explicit temporal information given to the ANN (i.e., only inputs of annual mean maps), the ANN still needs to learn patterns of forced climate signals which evolve through time for correctly predicting the order of the number of years since 2035. By design, this prediction task is similar to recent studies which showed that ANNs can spatially leverage regional climate information to predict the year of a climate map (e.g., Barnes et al., 2019; Labe and Barnes, 2021; Madakumbura et al., 2021; Rader et al., 2022). More details on the ANN architecture can be found in text S3 and in figures S5 to S8.

3.3. Explainable Machine Learning

We are interested in not only the SCI detection prediction itself, but also in identifying the relevant climate patterns used by the machine learning models. To reveal these regions, we consider a method of feature attribution for each of the logistic regression and ANN models. Attribution describes the contribution of the input features to the overall output. Despite an increasing number of explainable machine learning methods adopted for various climate science applications (e.g., Toms et al., 2020; Sonnewald and Lguensat, 2021; Labe and Barnes, 2022; Molina et al., 2021), we focus on two conceptually simple methods that we refer to as contribution maps. For identifying the significant regions to determine whether a climate map is from the SSP2-4.5 or SAI simulation, we consider contribution maps by multiplying the logistic regression model weights by the input values for every location on the map. As a corresponding approach, we evaluate contribution maps for the ANNs by using the input*gradient method (Shrikumar et al., 2016; Shrikumar et al., 2017). Input*gradient is calculated from the local gradient multiplied by the input map itself, which Mamalakis et al. (2022) found to perform well against other explainability methods on a benchmark climate dataset for a similar kind of problem. In both approaches, positive contributions can be interpreted as relevant areas that helped to push the machine learning models toward their final prediction.

4. Results

4.1. Detecting the regional emergence of SAI

The area-averaged time series of temperature is shown in figure s9 for each region in the SAI and SSP2-4.5 simulations. Due to the dominant influence of external forcing from increasing anthropogenic greenhouse gases, warming is evident in all 9 regions in the SSP2-4.5 scenario. The largest warming is found in the polar regions (figures s9(d) and (e)), although there is also greater ensemble spread. In comparison, after the injection of stratospheric aerosols in 2035 in the SAI simulation, the ensemble mean temperature exhibits little to no forced trend in all regions.

Although there are differences in the ensemble mean trends of temperature between SAI and SSP2-4.5, the ensemble member spread overlaps in all regions for at least the first 10 years after the start of SCI. This suggests that internal variability alone could inhibit determining whether a region is observing a SAI or SSP2-4.5 world (Keys et al., 2022; NASEM, 2021). To investigate this question, we utilize our first machine learning method. As described earlier, we input a single annual mean map of temperature for each region and output whether it is from a SAI or SSP2-4.5 world. The results of the logistic regression predictions are shown in figure 2 for global land areas, and each year from 2035 to 2069 is denoted with a shaded circle. The transparency of each circle is determined by the logistic regression model confidence. The logistic regression model achieves an accuracy of 92.6% on the testing ensemble member predictions of temperature. Even more striking, the logistic regression model achieves perfect accuracy after approximately the first 5 years of SCI injection. In other words, the logistic regression model is able to distinguish whether a global map of temperature is under the influence of SCI well within the first decade, despite the influence of internal climate variability (figure s9(a)).

Similarly, the annual mean precipitation is displayed in figure s10 for each of the 9 regions, and the logistic regression testing predictions are displayed in figure 2. Unlike the ensemble mean trends for temperature, we find notably smaller forced changes in precipitation in both the SAI and SSP2-4.5 simulations (figure s10). Although the ensemble mean is usually slightly wetter in SSP2-4.5 (figures s10(a) to (f)), the spread of annual mean precipitation across ensemble members overlaps in all regions through 2069. Despite this, the logistic regression model is once again able to accurately distinguish global maps of precipitation of SAI from SSP2-4.5 within the first 5 years of SCI injection (figure 2). The overall accuracy for precipitation is 91.4%, but the model confidence is at times lower for a few individual years (e.g., 2044 for SSP2-4.5), which we attribute to interannual variability (figure S10(a)).

To understand how the logistic regression model is making accurate predictions, we turn to the explainability method using contribution maps (input×weights). Fig-

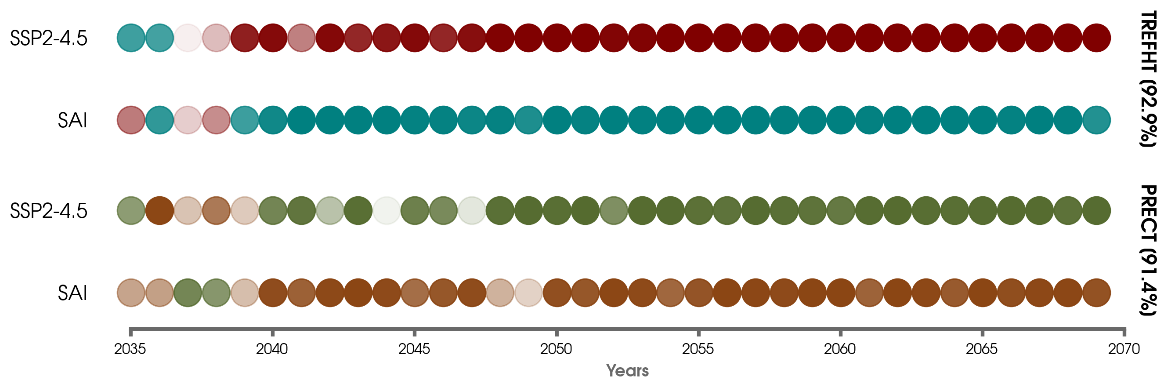

Figure 2. logistic regression model predictions for the single testing ensemble member of the SSPS-4.5 scenario and of the SAI scenario for annual mean maps of temperature (top) and precipitation (bottom) from 2035 to 2069. Predictions of temperature are denoted with a red circle for SSP2-4.5 and a blue circle for SAI. Predictions of precipitation are denoted with a green circle for SSP2-4.5 and a brown circle for SAI. The color transparency indicates the logistic regression model confidence for each prediction, which are then scaled between 0 (light shading) to 1 (darkest shading). The total accuracy score for the testing ensemble members is indicated on the right label for temperature and precipitation, respectively.

ure 3(a) shows the contribution map composite for temperature predictions in the SAI simulation, which are averaged over years 2045 to 2069. As discussed in section 3.3, positive contributions in figure 3(a) can be interpreted as regions that pushed the logistic regression model to make its classification. We find that areas in Greenland, southern South America, eastern Africa, and eastern Australia are all important regions for driving the logistic regression model to determine that a global land map is from a world under the influence of SCI. Next, we compare this contribution map with signal-to-noise ratios in figure s3(b), which are calculated as the SAI ensemble mean trend over 2045 to 2069 (forced response) divided by the standard deviation across the individual ensemble member trends (internal variability). We find strikingly similar spatial patterns of higher signal-to-noise between many of the same regions with positive contributions for the logistic regression model. In agreement with Barnes et al. (2022), this suggests that the logistic regression model is learning patterns of temperature signals to detect the influence of SCI. Moreover, we note that not all areas of higher positive contributions are associated with higher signal-to-noise, such as for positive contributions across Mexico and the southern United States. This means that the logistic regression model is leveraging spatial temperature signals across each map, rather than only learning point-by-point statistics.

The contribution maps composited over the entire 2035 to 2069 period are in figure s11 for temperature (a, c) and precipitation (b, d). The temperature contributions for both SAI and SSP2-4.5 predictions are similar to the one displayed in figure 3(a), which reinforces the importance of those regions as reliable indicators for detecting SCI within

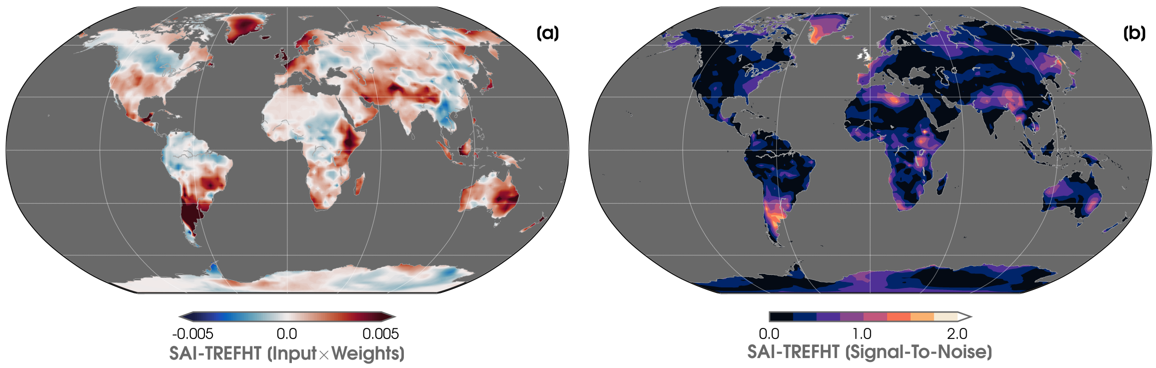

Figure 3. (a) Contribution map (input×weights) for the logistic regression model predictions of the SAI testing ensemble member averaged over 2045 to 2069 for temperature. (b) Signal-to-noise ratio (SNR) map of annual mean temperature over 2045 to 2069. SNR is defined as the absolute value of the ensemble mean trend (forced response) divided by the standard deviation of trends across individual ensemble members (internal variability).

the ARISE-SAI-1.5 experiment. For maps of precipitation, positive contributions for detecting SAI (figure s11(b)) are particularly prominent for areas in northern Canada, southern Greenland, northern South America, and south-central Africa. In addition, parts of eastern Siberia, central Asia, and west-central North America are locations of higher positive contributions for pushing the logistic regression model to predict maps from SSP2-4.5.

Finally, we repeat this exercise by separately training logistic regression models for the other 8 regions using temperature and precipitation. For brevity, we only show the explainability composites using the global contribution maps as displayed above. Similar to the global predictions in figure 2, a single circle is displayed for each annual mean map of either temperature or precipitation in figure 3. Accurate predictions of detecting whether a temperature map is from SAI or SSP2-4.5 are made within the first decade for each hemisphere and across the Tropics. However, for smaller spatial regions (i.e., Southeast Asia, Amazon, and Central Africa) or those areas with higher interannual variability (i.e., Arctic and Antarctic) (figure s2(a)), a greater range in the timing of accurate predictions is evident. In general, the logistic regression model is able to determine the correct climate model simulation for the majority of the years. For example, the logistic regression predictions of temperature are correct after 2039 in the Arctic, except for one incorrect prediction in 2069. There is also lower model confidence in the predictions for the Antarctic, Southeast Asia, and the Amazon until about the last 5-10 years of the ARISE-SAI-1.5 experiment. In summary, we conclude that the impacts of SCI on regional temperature are detectable using the logistic regression model, but regions with greater variability and smaller spatial spaces can lead to occasional misclassifications, especially prior to about 2060.

297

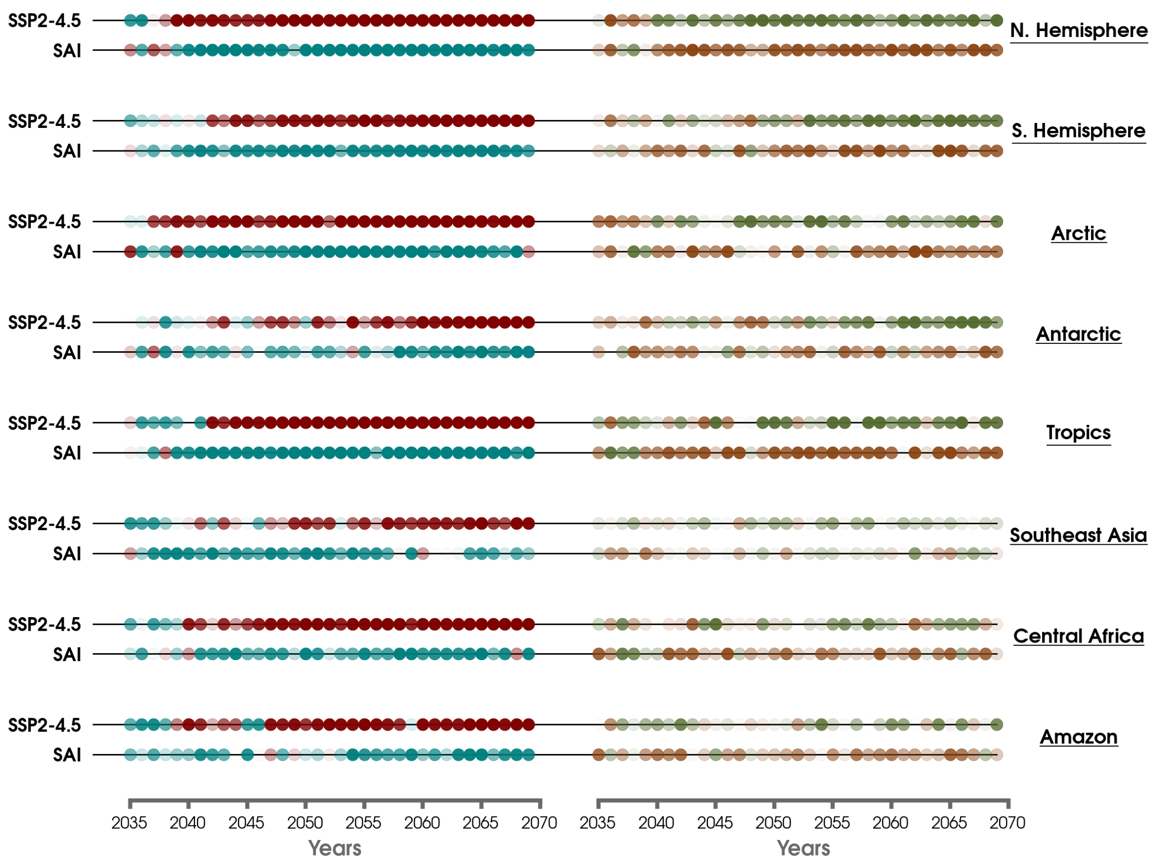

Figure 4. As in Figure 2, but for logistic regression models using input maps of temperature (left column) and precipitation (right column) in the Northern Hemisphere, Southern Hemisphere, Arctic, Antarctic, Tropics, Southeast Asia, Central Africa, and Amazon (top to bottom).

There is less overall skill for logistic regression predictions using precipitation. Indeed, the model confidence is especially low (i.e., closer to 0.5) for its precipitation predictions using only input maps of Southeast Asia, Central Africa, and the Amazon. In contrast, we find higher skill for logistic regression predictions in the Northern Hemisphere (e.g., perfect accuracy after 2039) and for the Tropics. Looking more closely at the timeseries of the regional annual mean precipitation in figure s10, we find the detectability of SCI is higher in the logistic regression predictions than might be inferred given the similarities in the SAI and SSP2-4.5 ensemble member spreads, like in the Tropics (figure s10(f)). This suggests that for precipitation, which has a much weaker response to external forcing, that there are some regional patterns of climate indicators that the logistic regression model is learning in order to make accurate predictions for either the SAI or SSP2-4.5 scenarios.

4.2. Time-evolving climate signals from SAI

So far, we've shown the influences of SCI are detectable on single global maps of annual mean temperature and precipitation. This result is also found for some geographical regions. Given these findings, we now ask the question whether a machine learning model can determine when SCI was first initiated, and thus it considers the time-evolving impacts of SCI on regional climate patterns. To address this more difficult prediction task, we use an ANN, which can further consider any nonlinearities in the evolution of climate signals. We only focus on regional data from the SAI simulation for this problem. Since the ANN is not explicitly given any temporal information in its input, it must therefore learn the timing of climate indicators for this regression task (i.e., the number of years since 2035).

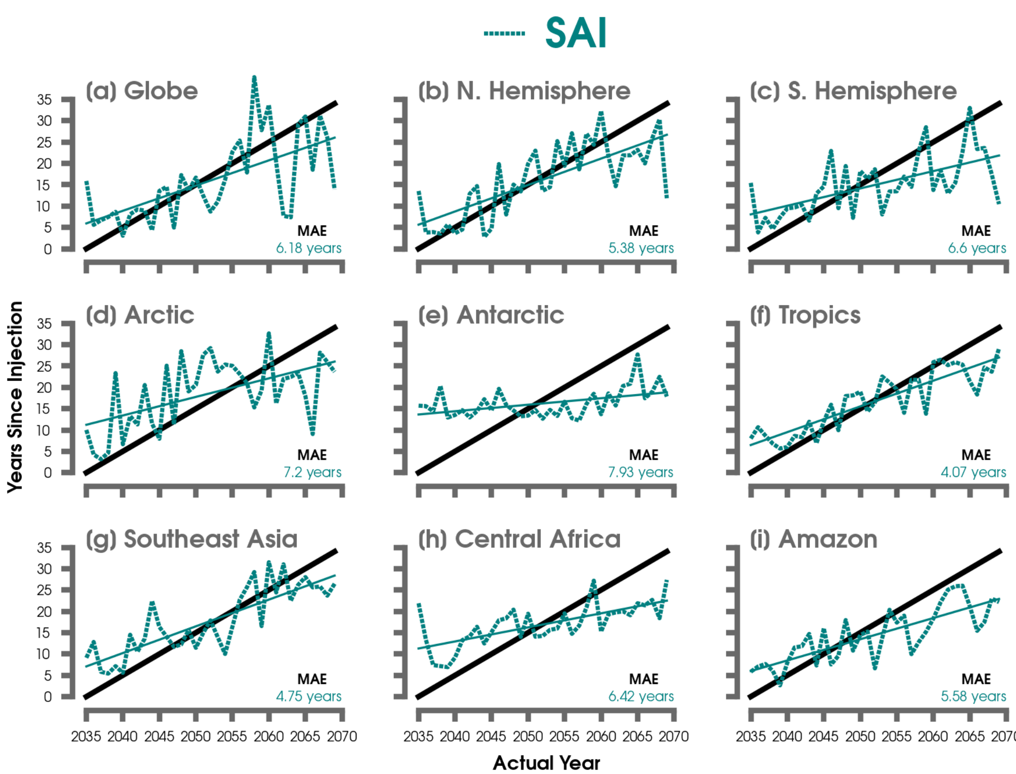

Figure 5. Predictions of the number of years since SAI injection by the ANN for the single SAI testing ensemble member of temperature for (a) global maps, (b) the Northern Hemisphere, (c) the Southern Hemisphere, (d) the Arctic, (e) the Antarctic, (f) the Tropics, (g) Southeast Asia, (h) Central Africa, (i) and the Amazon. The mean absolute error (MAE) for each region is included in the lower right-hand corner. The blue solid lines shows the linear least squares fit through the predictions of each regional ANN. The 1:1 lines (or perfect predictions) are shown in black.

First, we evaluate the spatial variability of the SAI ensemble mean trends of temperature and precipitation in figures s12 and s13, respectively. For completeness, we also include the ensemble mean trends for SSP2-4.5. Although cooling is found in most regions of the SAI simulation within the first decade since aerosol injection (figure s12(a), there is also spatial variability. This includes warming in parts of the extratropical Northern Hemisphere. Rather than suggesting that this is a robust, forced response to SCI, it is more likely that this is simply a reflection of internal variability, which is discussed in more detail in Keys et al. (2022) and is also demonstrated by the large spread of ensemble member trends in figure s14. Furthermore, there is large variability in precipitation trends in the first decade since SCI initiation (figure s13(a)), but weaker trends in the longer 2045 to 2069 period (figure s13(d)). We do note that one area with more consistent precipitation change is in the southeastern Amazon with an overall drying trend, but there is again a large spread across individual ensemble member trends (figures s14(c) and s14(g)).

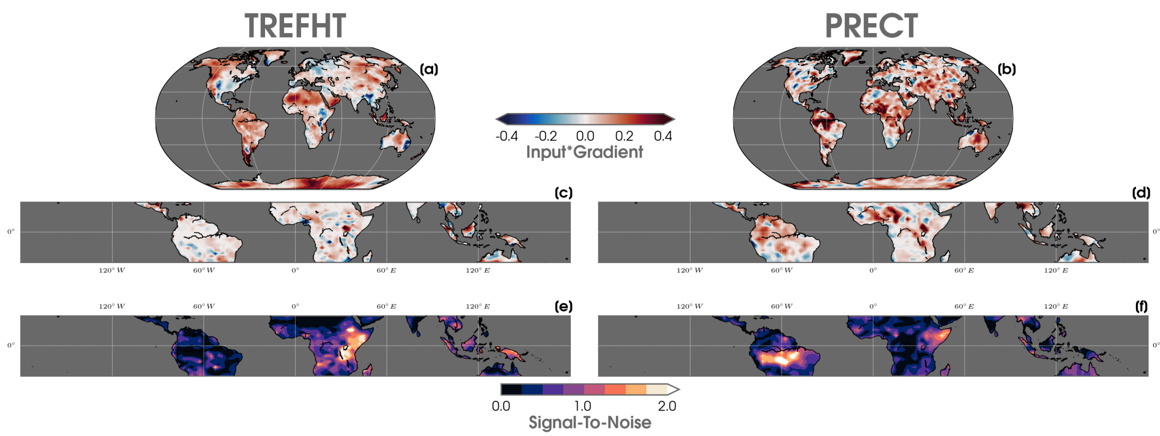

Figure 6. Contribution maps using the input*gradient method averaged over 2035 to 2069 for the ANN testing predictions for global maps of (a) temperature and (b) precipitation. (c-d) As in (a-b), but for input maps using only the Tropics. The composites are scaled by each map's maximum value (in absolute terms) to improve visual clarity. (d-e) As in Figure 3b, but for SNR averaged over 2035 to 2069 for temperature and precipitation in the Tropics, respectively.

Now we turn to the ANN prediction problem for more insights on the timing of possible climate signals. The results for a single testing ensemble member are shown for temperature in figure 5 (dashed blue line) compared to the 1:1 solid black line (or 'perfect prediction'). The corresponding training ensemble member predictions are displayed in figure s15. Overall, we find a strongly positive slope for the SAI predictions using all regional input maps, except for the Antarctic (figure 5(e)). Although there is a wide range in mean absolute error (MAE) scores, the ANN is still able to learn a time-evolving signal for temperature, as reflected by the slope of the prediction lines and higher correlation coefficient (figure s7). We are more interested in how well the ANN captures the correct order of the years, rather than identifying perfect yearly predictions. We find predictions close to the 1:1 line even for some smaller input regions, including Southeast Asia (figure 5(g)) and the Tropics (figure 5(f)). In all regions, the

ANN predicts a slower timing of emergence of climate signals (i.e., predicted slope below 1).

To understand where the ANN is looking to make the temperature predictions, we evaluate contribution maps using the input*gradient method for global land maps (figure 6(a)) and for inputs using only the Tropics (figure 6(c)). The respective ANN contribution maps are composited over all years from 2035 to 2069. Areas of positive contributions are evident across much of the Antarctic, South America, northern Africa, and northwestern North America. Notably, these regions differ from the climate patterns leveraged by the logistic regression model predictions (e.g., figure S11(a) and S11(c)), but this could be a result of comparing different machine learning methods, different prediction tasks, and the greater variability in prediction error for the ANN. The composited contribution maps for the input fields of temperature in the Tropics are noisier and more difficult to interpret in figure 6(c), but some areas of positive contribution are seen across islands in Indonesia that correspond to locations of higher signal-to-noise ratios (figure s6(e)).

Finally, we utilize this ANN framework using input maps of regional precipitation. The predictions for the testing ensemble member are shown in figure s16, and the corresponding training ensemble predictions are included in figure s17. The contribution maps are shown for inputs of global maps in figure 6(b) and for maps of the Tropics in figure 6(d). Unlike for temperature, the ANN is unable to learn patterns of reliable precipitation signals to correctly predict the order of the years since the deployment SCI in all regions. The ANN also suffers from overfitting on the training data. For the testing ensemble member, higher positive contributions are found across northern South America and central Africa using both global and tropical maps of precipitation as inputs to the ANN. However, we cannot completely determine whether these regions and lack of prediction skill is from the limited training data, which could prevent the ANN from filtering the relevant spatial signals from the background noise.

5. Discussion and Conclusions

A key recommendation from NASEM (2021) was that research was needed to better understand the detection and attribution of climate-related impacts from SCI. While it is likely that satellite remote-sensing observations would be able to quickly detect changes in aerosol optical depth (Li et al., 2022), it is still uncertain whether responses in the climate system would be distinguishable from internal variability. This is an important question at smaller regional scales, given the potential societal impacts from even small changes to temperature extremes or the hydrological cycle. In this study, we begin to assess these questions by employing several machine learning methods to evaluate whether the regional effects of temperature and precipitation would be detectable under a plausible future SCI scenario.

Despite a much weaker external forcing scenario than was considered in Barnes et al. (2022), we find similar results for the accurate detection of temperature and precipitation impacts over global lands areas by the logistic regression model. This occurs within approximately the first decade of SCI initiation. We also find utility in training an ANN to identify when SCI was started simply by inputting annual mean maps of temperature. Using the contribution maps as explainability tools for the machine learning methods, we show that the logistic regression and ANN models are leveraging combinations of climate signals across the maps in order to make correct predictions. While these patterns are sometimes associated with areas of higher signal-to-noise, this is not always the case, especially for the more complex ANN approach. In fact, one advantage of this data-driven approach is that we are not restricted to linear point-by-point statistics, as in many signal-to-noise metrics.

There is a much wider range of skill for predicting the emergence in smaller geographic regions, especially for precipitation. For example, we do not find any skill in detecting whether a map of precipitation is from either SSP2-4.5 or SAI over Southeast Asia. This result is not surprising given the challenges in disentangling the influences of anthropogenic aerosols, greenhouse gases, and internal variability on the forced response of regional precipitation (Lin et al., 2016; Deser et al., 2020; Ha et al., 2020). As shown in Keys et al. (2022), internal variability can modulate or altogether mask the influences of SCI in the ARISE-SAI-1.5 simulation. Nonetheless, we cannot rule out higher prediction skill with more available training data. Here we are only using 7 ensemble members (n=10) from each of SAI and SSP2-4.5 simulations to train and validate the logistic regression and ANN models. This may not be enough ensemble members to disentangle the signal from the noise (Milinski et al., 2020), and consequently it can limit the amount of information for the machine learning models to learn the combined regional climate change patterns due to SCI amidst the background noise. Finally, we note that our results are restricted to one climate model and are susceptible to any inherent model biases in CESM2(WACCM6). As future large ensembles are developed for evaluating SCI scenarios (Visioni and Robock, 2022), it will be important to compare data-driven approaches for detecting temperature and precipitation impacts in other global climate models.

Conflict of interest

The authors declare no conflicts of interest relevant to this study.

Data Availability Statement

Climate model experiments used in this study are freely available from the Climate Data Gateway at NCAR for ARISE-SAI-1.5 (`https://doi.org/10.5065/9kcn-9y79`) and

CESM2-WACCM6-SSP2-4.5 (`https://doi.org/10.26024/0cs0-ev98`) (Richter and Visioni, 2022). Additional climatological statistics for ARISE-SAI-1.5 can be found from the NCAR Climate Variability Diagnostics Package for Large Ensembles (CVDP; Phillips et al., 2020) at `https://project.cgd.ucar.edu/projects/ARISE-SAI-1.5/CVDP-LE/`.

Software tools from NCO v4.9.3 (Zender, 2008), CDO v1.9.8 (Schulzweida, 2019), and NCL v6.2.2 (NCAR, 2019) were used for initial data preprocessing and evaluation. Computer code for the exploratory data analysis, plotting scripts, logistic regression architecture, artificial neural network architecture, and explainability methods are available at `https://github.com/zmlabe/SAI` using Python v3.7.6 (Rossum and Drake, 2009). *(Reviewers, please note that this GitHub URL will transition to an archived-DOI repository at Zenodo if this paper is considered for publication).* Additional necessary Python packages for this study include Numpy v1.19 (Harris et al., 2020), SciPy v1.4.1 (Virtanen et al., 2020), Scikit-learn v0.24.2 (Pedregosa et al., 2011), and TensorFlow v2.7.0 (Abadi et al., 2016). Lastly, Matplotlib v3.2.2 (Hunter, 2007) was used for generating figures with colormaps from cmocean v2.0 (Thyng et al., 2016), CMasher v1.6.0 (van der Velden, 2020), and Palettable's cubehelix v3.3.0 (Green, 2011).

Acknowledgments

This work was supported by Defense Advanced Research Projects Agency (DARPA) Grant No. HR00112290071. The views expressed here do not necessarily reflect the positions of the U.S. government. We also would like to acknowledge high-performance computing and storage from NCAR's Computational and Information Systems Laboratory's (CISL) Cheyenne (`doi:10.5065/D6RX99HX`) for the support of the ARISE-SAI-1.5 simulations.

References

Abadi, M., Barham, P., Chen, J., Chen, Z., Davis, A., Dean, J., Devin, M., Ghemawat, S., Irving, G., Isard, M., Kudlur, M., Levenberg, J., Monga, R., Moore, S., Murray, D. G., Steiner, B., Tucker, P., Vasudevan, V., Warden, P., Wicke, M., Yu, Y. and Zheng, X. (2016). Tensorflow: A system for large-scale machine learning.

Abatayo, A. L., Bosetti, V., Casari, M., Ghidoni, R. and Tavoni, M. (2020). Solar geoengineering may lead to excessive cooling and high strategic uncertainty, *Proceedings of the National Academy of Sciences of the United States of America* **117**: 13393–13398.
URL: *https://www.pnas.org/doi/abs/10.1073/pnas.1916637117*

Barnes, E. A., Hurrell, J. W., Ebert-Uphoff, I., Anderson, C. and Anderson, D. (2019). Viewing forced climate patterns through an ai lens, *Geophysical Research Letters* **46**: 13389–13398.
URL: *https://onlinelibrary.wiley.com/doi/abs/10.1029/2019GL084944*

Barnes, E. A., Hurrell, J. W. and Sun, L. (2022). Detecting changes in global extremes under the glens-sai climate intervention strategy, *Geophysical Research Letters* p. e2022GL100198.
URL: *https://onlinelibrary.wiley.com/doi/full/10.1029/2022GL100198*

Burgess, M. G., Ritchie, J., Shapland, J. and Pielke, R. (2020). Ipcc baseline scenarios have over-projected co2 emissions and economic growth, *Environmental Research Letters* **16**: 014016.
URL: *https://iopscience.iop.org/article/10.1088/1748-9326/abcdd2*

Burns, E. T., Flegal, J. A., Keith, D. W., Mahajan, A., Tingley, D. and Wagner, G. (2016). What do people think when they think about solar geoengineering? a review of empirical social science literature, and prospects for future research, *Earth's Future* **4**: 536–542.
URL: *https://onlinelibrary.wiley.com/doi/full/10.1002/2016EF000461*

Carlson, C. J. and Trisos, C. H. (2018). Climate engineering needs a clean bill of health, *Nature Climate Change 2018 8:10* **8**: 843–845.
URL: *https://www.nature.com/articles/s41558-018-0294-7*

Cheng, L., von Schuckmann, K., Abraham, J. P., Trenberth, K. E., Mann, M. E., Zanna, L., England, M. H., Zika, J. D., Fasullo, J. T., Yu, Y., Pan, Y., Zhu, J., Newsom, E. R., Bronselaer, B. and Lin, X. (2022). Past and future ocean warming, *Nature Reviews Earth and Environment* pp. 1–19.
URL: *https://www.nature.com/articles/s43017-022-00345-1*

Clarke, B., Otto, F., Stuart-Smith, R. and Harrington, L. (2022). Extreme weather impacts of climate change: an attribution perspective, *Environmental Research: Climate* **1**: 012001.
URL: *https://iopscience.iop.org/article/10.1088/2752-5295/ac6e7d https://iopscience.iop.org/article/10.1088/2752-5295/ac6e7d/meta*

Danabasoglu, G., Lamarque, J.-F., Bacmeister, J., Bailey, D. A., DuVivier, A. K., Edwards, J., Emmons, L. K., Fasullo, J., Garcia, R., Gettelman, A., Hannay, C., Holland, M. M., Large, W. G., Lauritzen, P. H., Lawrence, D. M., Lenaerts, J. T. M., Lindsay, K., Lipscomb, W. H., Mills, M. J., Neale, R., Oleson, K. W., Otto-Bliesner, B., Phillips, A. S., Sacks, W., Tilmes, S., van Kampenhout, L., Vertenstein, M., Bertini, A., Dennis, J., Deser, C., Fischer, C., Fox-Kemper, B., Kay, J. E., Kinnison, D., Kushner, P. J., Larson, V. E., Long, M. C., Mickelson, S., Moore, J. K., Nienhouse, E., Polvani, L., Rasch, P. J. and Strand, W. G. (2020). The community earth system model version 2 (cesm2), *Journal of Advances in Modeling Earth Systems* **12**: e2019MS001916.
URL: *https://agupubs.onlinelibrary.wiley.com/doi/10.1029/2019MS001916*

Davis, S. J., Lewis, N. S., Shaner, M., Aggarwal, S., Arent, D., Azevedo, I. L., Benson, S. M., Bradley, T., Brouwer, J., Chiang, Y. M., Clack, C. T., Cohen, A., Doig, S., Edmonds, J., Fennell, P., Field, C. B., Hannegan, B., Hodge, B. M., Hoffert, M. I., Ingersoll, E., Jaramillo, P., Lackner, K. S., Mach, K. J., Mastrandrea, M., Ogden, J., Peterson, P. F., Sanchez, D. L., Sperling, D., Stagner, J., Trancik, J. E., Yang, C. J. and Caldeira, K. (2018). Net-zero emissions energy systems, *Science* **360**.
URL: *https://www.science.org/doi/10.1126/science.aas9793*

de Kleijne, K., Hanssen, S. V., van Dinteren, L., Huijbregts, M. A., van Zelm, R. and de Coninck, H. (2022). Limits to paris compatibility of co2 capture and utilization, *One Earth* **5**: 168–185.

Deser, C., Phillips, A. S., Simpson, I. R., Rosenbloom, N., Coleman, D., Lehner, F., Pendergrass, A. G. and Stevenson, S. (2020). Isolating the evolving contributions of anthropogenic aerosols and greenhouse gases: A new cesm1 large ensemble community resource, *Journal of Climate* **33**: 7835–7858.
URL: *https://doi.org/10.1175/JCLI-D-20-*

Dunn, R. J. H., Aldred, F., Gobron, N., Miller, J. B., Willett, K. M., Ades, M., Adler, R., Richard, P. A., Allan, R., Anderson, J., Argüez, A., Arosio, C., Augustine, J. A., Azorin-Molina, C., Barichivich, J., Beck, H. E., Becker, A., Bellouin, N., Benedetti, A., Berry, D. I., Blenkinsop, S., Bock, O., Bodin, X., Bosilovich, M. G., Boucher, O., Buehler, S. A., Calmettes, B., Carrea, L., Castia, L., Christiansen, H. H., Christy, J. R., Chung, E.-S., Coldewey-Egbers, M., Cooper, O. R., Cornes, R. C., Covey, C., Cretaux, J.-F., Crotwell, M., Davis, S. M., de Jeu, R. A. M., Degenstein, D., Delaloye, R., Girolamo, L. D., Donat, M. G., Dorigo, W. A., Durre, I., Dutton, G. S., Duveiller, G., Elkins, J. W., Fioletov, V. E., Flemming, J., Foster, M. J., Frith, S. M.,

Froidevaux, L., Garforth, J., Gentry, M., Gupta, S. K., Hahn, S., Haimberger, L., Hall, B. D., Harris, I., Hemming, D. L., Hirschi, M., pen (Ben) Ho, S., Hrbacek, F., Hubert, D., Hurst, D. F., Inness, A., Isaksen, K., John, V. O., Jones, P. D., Junod, R., Kaiser, J. W., Kaufmann, V., Kellerer-Pirklbauer, A., Kent, E. C., Kidd, R., Kim, H., Kipling, Z., Koppa, A., Kraemer, B. M., Kratz, D. P., Lan, X., Lantz, K. O., Lavers, D., Loeb, N. G., Loyola, D., Madelon, R., Mayer, M., McCabe, M. F., McVicar, T. R., Mears, C. A., Merchant, C. J., Miralles, D. G., Moesinger, L., Montzka, S. A., Morice, C., Mösinger, L., Mühle, J., Nicolas, J. P., Noetzli, J., Noll, B., O'Keefe, J., Osborn, T. J., Park, T., Pasik, A. J., Pellet, C., Pelto, M. S., Perkins-Kirkpatrick, S. E., Petron, G., Phillips, C., Po-Chedley, S., Polvani, L., Preimesberger, W., Rains, D. G., Randel, W. J., Rayner, N. A., Rémy, S., Ricciardulli, L., Richardson, A. D., Robinson, D. A., Rodell, M., Rodríguez-Fernández, N. J., Rosenlof, K., Roth, C., Rozanov, A., Rutishäuser, T., Sánchez-Lugo, A., Sawaengphokhai, P., Scanlon, T., Schenzinger, V., Schlegel, R. W., Sharma, S., Shi, L., Simmons, A. J., Siso, C., Smith, S. L., Soden, B. J., Sofieva, V., Sparks, T. H., Stackhouse, P. W., Steinbrecht, W., Stengel, M., Streletskiy, D. A., Sun-Mack, S., Tans, P., Thackeray, S. J., Thibert, E., Tokuda, D., Tourpali, K., Tye, M. R., van der A, R., van der Schalie, R., van der Schrier, G., van der Vliet, M., van der Werf, G. R., Vance, A., Vernier, J.-P., Vimont, I. J., Vömel, H., Vose, R. S., Wang, R., Weber, M., Wiese, D., Wilber, A. C., Wild, J. D., Wong, T., Woolway, R. I., Zhou, X., Yin, X., Zhao, G., Zhao, L., Ziemke, J. R., Ziese, M. and Zotta, R. M. (2021). Global climate, *Bulletin of the American Meteorological Society* **102**: S11–S142.
URL: *https://journals.ametsoc.org/view/journals/bams/102/8/BAMS-D-21-0098.1.xml*

Dvorak, M. T., Armour, K. C., Frierson, D. M., Proistosescu, C., Baker, M. B. and Smith, C. J. (2022). Estimating the timing of geophysical commitment to 1.5 and 2.0c of global warming, *Nature Climate Change 2022 12:6* **12**: 547–552.
URL: *https://www.nature.com/articles/s41558-022-01372-y*

Gettelman, A., Mills, M. J., Kinnison, D. E., Garcia, R. R., Smith, A. K., Marsh, D. R., Tilmes, S., Vitt, F., Bardeen, C. G., McInerny, J., Liu, H. L., Solomon, S. C., Polvani, L. M., Emmons, L. K., Lamarque, J. F., Richter, J. H., Glanville, A. S., Bacmeister, J. T., Phillips, A. S., Neale, R. B., Simpson, I. R., DuVivier, A. K., Hodzic, A. and Randel, W. J. (2019). The whole atmosphere community climate model version 6 (waccm6), *Journal of Geophysical Research: Atmospheres* **124**: 12380–12403.
URL: *https://onlinelibrary.wiley.com/doi/full/10.1029/2019JD030943*

Green, D. A. (2011). A colour scheme for the display of astronomical intensity images, *Bulletin of the Astronomical Society of India* **39**.

Ha, K. J., Kim, B. H., Chung, E. S., Chan, J. C. and Chang, C. P. (2020). Major factors of global and regional monsoon rainfall changes: natural versus anthropogenic forcing, *Environmental Research Letters* **15**: 034055.
URL: *https://iopscience.iop.org/article/10.1088/1748-9326/ab7767/meta*

Harris, C. R., Millman, K. J., van der Walt, S. J., Gommers, R., Virtanen, P., Cournapeau, D., Wieser, E., Taylor, J., Berg, S., Smith, N. J., Kern, R., Picus, M., Hoyer, S., van Kerkwijk, M. H., Brett, M., Haldane, A., del Río, J. F., Wiebe, M., Peterson, P., Gérard-Marchant, P., Sheppard, K., Reddy, T., Weckesser, W., Abbasi, H., Gohlke, C. and Oliphant, T. E. (2020). Array programming with numpy, *Nature* **585**: 357.
URL: *https://doi.org/10.1038/s41586-020-2649-2*

Hausfather, Z. and Peters, G. P. (2020). Rcp8.5 is a problematic scenario for near-term emissions.

Hsu, C. W. and Velicogna, I. (2017). Detection of sea level fingerprints derived from grace gravity data, *Geophysical Research Letters* **44**: 8953–8961.
URL: *https://onlinelibrary.wiley.com/doi/full/10.1002/2017GL074070*

Hunter, J. D. (2007). Matplotlib: A 2d graphics environment, *Computing in Science and Engineering* **9**: 99–104.

Hurrell, J. W., Holland, M. M., Gent, P. R., Ghan, S., Kay, J. E., Kushner, P. J., Lamarque, J. F., Large, W. G., Lawrence, D., Lindsay, K., Lipscomb, W. H., Long, M. C., Mahowald, N., Marsh, D. R., Neale, R. B., Rasch, P., Vavrus, S., Vertenstein, M., Bader, D., Collins, W. D., Hack, J. J., Kiehl, J. and Marshall, S. (2013). The community earth system model: A framework for collaborative research, *Bulletin of the American Meteorological Society* **94**.

IPCC (2018). Ipcc special report on global warming of 1.5c, *IPCC* **2**.

IPCC, Masson-Delmotte, V., Zhai, P., Pirani, A., Connors, S. L., Péan, C., Berger, S., Caud, N., Chen, Y., Goldfarb, L., Gomis, M. I., Huang, M., Leitzell, K., Lonnoy, E., Matthews, J. B. R., Maycock, T. K., Waterfield, T., Yelekçi, O., Yu, R. and B., Z. (2021). Climate change 2021: The physical science basis. contribution of working group i to the sixth assessment report of the intergovernmental panel on climate change.

Irvine, P. J., Kravitz, B., Lawrence, M. G. and Muri, H. (2016). An overview of the earth system science of solar geoengineering, *Wiley Interdisciplinary Reviews: Climate Change* **7**: 815–833.
URL: *https://onlinelibrary.wiley.com/doi/full/10.1002/wcc.423*

Keys, P. W., Barnes, E. A., Diffenbaugh, N. S., Hurrell, J. W. and Bell, C. M. (2022). Potential for perceived failure of stratospheric aerosol injection deployment, *Proceedings of the National Academy of Sciences* **119**: e2210036119.
URL: *https://www.pnas.org/doi/abs/10.1073/pnas.2210036119*

Kravitz, B. and MacMartin, D. G. (2020). Uncertainty and the basis for confidence in solar geoengineering research.

Kravitz, B., Macmartin, D. G., Mills, M. J., Richter, J. H., Tilmes, S., Lamarque, J. F., Tribbia, J. J. and Vitt, F. (2017). First simulations of designing stratospheric sulfate aerosol geoengineering to meet multiple simultaneous climate objectives, *Journal of Geophysical Research: Atmospheres* **122**: 12,616–12,634.
URL: *https://onlinelibrary.wiley.com/doi/full/10.1002/2017JD026874*

Kravitz, B., Robock, A., Boucher, O., Schmidt, H., Taylor, K. E., Stenchikov, G. and Schulz, M. (2011). The geoengineering model intercomparison project (geomip), *Atmospheric Science Letters* **12**: 162–167.
URL: *https://onlinelibrary.wiley.com/doi/full/10.1002/asl.316*

Kravitz, B., Robock, A., Tilmes, S., Boucher, O., English, J. M., Irvine, P. J., Jones, A., Lawrence, M. G., MacCracken, M., Muri, H., Moore, J. C., Niemeier, U., Phipps, S. J., Sillmann, J., Storelvmo, T., Wang, H. and Watanabe, S. (2015). The geoengineering model intercomparison project phase 6 (geomip6): Simulation design and preliminary results, *Geoscientific Model Development* **8**: 3379–3392.

Labe, Z. M. and Barnes, E. A. (2021). Detecting climate signals using explainable ai with single-forcing large ensembles, *Journal of Advances in Modeling Earth Systems* **13**: e2021MS002464.
URL: *https://agupubs.onlinelibrary.wiley.com/doi/10.1029/2021MS002464*

Labe, Z. M. and Barnes, E. A. (2022). Comparison of climate model large ensembles with observations in the arctic using simple neural networks, *Earth and Space Science* **9**: e2022EA002348.
URL: *https://doi.org/10.1029/2022EA002348*

Li, J., Carlson, B. E., Yung, Y. L., Lv, D., Hansen, J., Penner, J. E., Liao, H., Ramaswamy, V., Kahn, R. A., Zhang, P., Dubovik, O., Ding, A., Lacis, A. A., Zhang, L. and Dong, Y. (2022). Scattering and absorbing aerosols in the climate system, *Nature Reviews Earth and Environment* **3**: 363–379.
URL: *https://www.nature.com/articles/s43017-022-00296-7*

Lin, L., Wang, Z., Xu, Y. and Fu, Q. (2016). Sensitivity of precipitation extremes to radiative forcing of greenhouse gases and aerosols, *Geophysical Research Letters* **43**: 9860–9868.
URL: *https://agupubs.onlinelibrary.wiley.com/doi/10.1002/2016GL070869*

Liu, Z., Deng, Z., Davis, S. J., Giron, C. and Ciais, P. (2022). Monitoring global carbon emissions in 2021, *Nature Reviews Earth and Environment* **3**: 217–219.
URL: *https://www.nature.com/articles/s43017-022-00285-w*

MacMartin, D. G., Kravitz, B., Keith, D. W. and Jarvis, A. (2014). Dynamics of the coupled human-

climate system resulting from closed-loop control of solar geoengineering, *Climate Dynamics* **43**: 243–258.
URL: *https://link.springer.com/article/10.1007/s00382-013-1822-9*

MacMartin, D. G., Visioni, D., Kravitz, B., Richter, J. H., Felgenhauer, T., Lee, W. R., Morrow, D. R., Parson, E. A. and Sugiyama, M. (2022). Scenarios for modeling solar radiation modification, *Proceedings of the National Academy of Sciences of the United States of America* **119**: e2202230119.
URL: *https://www.pnas.org/doi/abs/10.1073/pnas.2202230119*

Madakumbura, G. D., Thackeray, C. W., Norris, J., Goldenson, N. and Hall, A. (2021). Anthropogenic influence on extreme precipitation over global land areas seen in multiple observational datasets, *Nature Communications 2021 12:1* **12**: 1–9.
URL: *https://www.nature.com/articles/s41467-021-24262-x*

Mahajan, A., Tingley, D. and Wagner, G. (2019). Fast, cheap, and imperfect? us public opinion about solar geoengineering, *Environmental Politics* **28**: 523–543.
URL: *https://www.tandfonline.com/doi/abs/10.1080/09644016.2018.1479101*

Mamalakis, A., Ebert-Uphoff, I. and Barnes, E. A. (2022). Neural network attribution methods for problems in geoscience: A novel synthetic benchmark dataset, *Environmental Data Science* **1**: e8.
URL: *https://www.cambridge.org/core/journals/environmental-data-science/article/neural-network-attribution-methods-for-problems-in-geoscience-a-novel-synthetic-benchmark-dataset/DDA562FC7B9A2B30710582861920860E*

Marvel, K., Cook, B. I., Bonfils, C. J., Durack, P. J., Smerdon, J. E. and Williams, A. P. (2019). Twentieth-century hydroclimate changes consistent with human influence, *Nature* **569**.

Matthews, H. D. and Wynes, S. (2022). Current global efforts are insufficient to limit warming to 1.5c, *Science* **376**: 1404–1409.
URL: *https://www.science.org/doi/10.1126/science.abo3378*

McKay, D. I., Staal, A., Abrams, J. F., Winkelmann, R., Sakschewski, B., Loriani, S., Fetzer, I., Cornell, S. E., Rockström, J. and Lenton, T. M. (2022). Exceeding 1.5c global warming could trigger multiple climate tipping points, *Science* **377**.
URL: *https://www.science.org/doi/10.1126/science.abn7950*

Meinshausen, M., Lewis, J., McGlade, C., Gütschow, J., Nicholls, Z., Burdon, R., Cozzi, L. and Hackmann, B. (2022). Realization of paris agreement pledges may limit warming just below 2c, *Nature* **604**: 304–309.
URL: *https://www.nature.com/articles/s41586-022-04553-z*

Milinski, S., Maher, N. and Olonscheck, D. (2020). How large does a large ensemble need to be?, *Earth System Dynamics* **11**: 885–901.
URL: *https://esd.copernicus.org/articles/11/885/2020/*

Mills, M. J., Richter, J. H., Tilmes, S., Kravitz, B., Macmartin, D. G., Glanville, A. A., Tribbia, J. J., Lamarque, J. F., Vitt, F., Schmidt, A., Gettelman, A., Hannay, C., Bacmeister, J. T. and Kinnison, D. E. (2017). Radiative and chemical response to interactive stratospheric sulfate aerosols in fully coupled cesm1(waccm), *Journal of Geophysical Research: Atmospheres* **122**.

Molina, M. J., Gagne, D. J. and Prein, A. F. (2021). A benchmark to test generalization capabilities of deep learning methods to classify severe convective storms in a changing climate, *Earth and Space Science* **8**: e2020EA001490.
URL: *https://agupubs.onlinelibrary.wiley.com/doi/10.1029/2020EA001490*

NASEM (2021). *Reflecting sunlight: Recommendations for Solar Geoengineering Research and Research Governance.*

NCAR (2019). The ncar command language (version 6.6.2).
URL: *http://dx.doi.org/10.5065/D6WD3XH5*

O'Neill, B. C., Tebaldi, C., Vuuren, D. P. V., Eyring, V., Friedlingstein, P., Hurtt, G., Knutti, R., Kriegler, E., Lamarque, J. F., Lowe, J., Meehl, G. A., Moss, R., Riahi, K. and Sanderson, B. M.

(2016). The scenario model intercomparison project (scenariomip) for cmip6, *Geoscientific Model Development* **9**: 3461–3482.

Pedregosa, F., Varoquaux, G., Gramfort, A., Michel, V., Thirion, B., Grisel, O., Blondel, M., Prettenhofer, P., Weiss, R., Dubourg, V., Vanderplas, J., Passos, A., Cournapeau, D., Brucher, M., Perrot, M. and Édouard Duchesnay (2011). Scikit-learn: Machine learning in python, *Journal of Machine Learning Research* **12**.

Peters, G. P. and Hausfather, Z. (2020). Emissions - the 'business as usual' story is misleading, *Nature* **577**.

Phillips, A. S., Deser, C., Fasullo, J., Schneider, D. P. and Simpson, I. R. (2020). Assessing climate variability and change in model large ensembles: A user's guide to the climate variability diagnostics package for large ensembles version 1.0.
URL: *https://opensky.ucar.edu/islandora/object/manuscripts:1001*

Pisoft, P., Sacha, P., Polvani, L. M., Añel, J. A., Torre, L. D. L., Eichinger, R., Foelsche, U., Huszar, P., Jacobi, C., Karlicky, J., Kuchar, A., Miksovsky, J., Zak, M. and Rieder, H. E. (2021). Stratospheric contraction caused by increasing greenhouse gases, *Environmental Research Letters* **16**: 064038.
URL: *https://iopscience.iop.org/article/10.1088/1748-9326/abfe2b*

Rader, J. K., Barnes, E. A., Ebert-Uphoff, I. and Anderson, C. (2022). Detection of forced change within combined climate fields using explainable neural networks, *Journal of Advances in Modeling Earth Systems* **14**: e2021MS002941.
URL: *https://onlinelibrary.wiley.com/doi/full/10.1029/2021MS002941*

Richter, J. H., Visioni, D., MacMartin, D. G., Bailey, D. A., Rosenbloom, N., Dobbins, B., Lee, W. R., Tye, M. and Lamarque, J.-F. (2022). Assessing responses and impacts of solar climate intervention on the earth system with stratospheric aerosol injection (arise-sai): protocol and initial results from the first simulations, *Geoscientific Model Development* **15**: 8221–8243.
URL: *https://gmd.copernicus.org/articles/15/8221/2022/*

Richter, J. and Visioni, D. (2022). Arise-sai-1.5: Assessing responses and impacts of solar climate intervention on the earth system with stratospheric aerosol injection, with cooling to 1.5c, *Zenodo* .
URL: *https://zenodo.org/record/6473775*

Robock, A. (2000). Volcanic eruptions and climate, *Reviews of Geophysics* **38**: 191–219.
URL: *https://onlinelibrary.wiley.com/doi/full/10.1029/1998RG000054*

Robock, A., Oman, L. and Stenchikov, G. L. (2008). Regional climate responses to geoengineering with tropical and arctic so2 injections, *Journal of Geophysical Research: Atmospheres* **113**: 16101.
URL: *https://onlinelibrary.wiley.com/doi/full/10.1029/2008JD010050*

Rossum, G. V. and Drake, F. L. (2009). *Python 3 Reference Manual*, CreateSpace.

Santer, B. D., Po-Chedley, S., Feldl, N., Fyfe, J. C., Fu, Q., Solomon, S., England, M., Rodgers, K. B., Stuecker, M. F., Mears, C., Zou, C.-Z., Bonfils, C. J. W., Pallotta, G., Zelinka, M. D., Rosenbloom, N. and Edwards, J. (2022). Robust anthropogenic signal identified in the seasonal cycle of tropospheric temperature, *Journal of Climate* **35**: 6075–6100.
URL: *https://journals.ametsoc.org/view/journals/clim/35/18/JCLI-D-21-0766.1.xml*

Schulzweida, U. (2019). Cdo user guide, *Zenodo* .
URL: *https://zenodo.org/record/2558193*

Shrikumar, A., Greenside, P. and Kundaje, A. (2017). Learning important features through propagating activation differences, Vol. 7.

Shrikumar, A., Greenside, P., Shcherbina, A. and Kundaje, A. (2016). Not just a black box: Learning important features through propagating activation differences, *34th International Conference on Machine Learning, ICML 2017* **7**.

Sippel, S., Meinshausen, N., Székely, E., Fischer, E., Pendergrass, A. G., Lehner, F. and Knutti, R. (2021). Robust detection of forced warming in the presence of potentially large climate variability, *Science Advances* **7**.

Slater, T., Lawrence, I. R., Otosaka, I. N., Shepherd, A., Gourmelen, N., Jakob, L., Tepes, P., Gilbert, L. and Nienow, P. (2021). Review article: Earth's ice imbalance, *Cryosphere* **15**.

Sonnewald, M. and Lguensat, R. (2021). Revealing the impact of global heating on north atlantic circulation using transparent machine learning, *Journal of Advances in Modeling Earth Systems* **13**: e2021MS002496.
URL: *https://agupubs.onlinelibrary.wiley.com/doi/10.1029/2021MS002496*

Thyng, K., Greene, C., Hetland, R., Zimmerle, H. and DiMarco, S. (2016). True colors of oceanography: Guidelines for effective and accurate colormap selection, *Oceanography* **29**: 9–13.
URL: *https://tos.org/oceanography/article/true-colors-of-oceanography-guidelines-for-effective-and-accurate-colormap*

Tilmes, S., Richter, J. H., Kravitz, B., Macmartin, D. G., Mills, M. J., Simpson, I. R., Glanville, A. S., Fasullo, J. T., Phillips, A. S., Lamarque, J. F., Tribbia, J., Edwards, J., Mickelson, S. and Ghosh, S. (2018). Cesm1(waccm) stratospheric aerosol geoengineering large ensemble project, *Bulletin of the American Meteorological Society* **99**: 2361–2371.
URL: *https://journals.ametsoc.org/view/journals/bams/99/11/bams-d-17-0267.1.xml*

Toms, B. A., Barnes, E. A. and Ebert-Uphoff, I. (2020). Physically interpretable neural networks for the geosciences: Applications to earth system variability, *Journal of Advances in Modeling Earth Systems* **12**.
URL: *https://onlinelibrary.wiley.com/doi/10.1029/2019MS002002*

UNFCCC (2015). What is the paris agreement?, *United Nations Climate Change* pp. 1–6.
URL: *https://unfccc.int/process-and-meetings/the-paris-agreement/what-is-the-paris-agreement*

van der Velden, E. (2020). Cmasher: Scientific colormaps for making accessible, informative and 'cmashing' plots, *Journal of Open Source Software* **5**: 2004.
URL: *https://joss.theoj.org/papers/10.21105/joss.02004*

Virtanen, P., Gommers, R., Oliphant, T. E., Haberland, M., Reddy, T., Cournapeau, D., Burovski, E., Peterson, P., Weckesser, W., Bright, J., van der Walt, S. J., Brett, M., Wilson, J., Millman, K. J., Mayorov, N., Nelson, A. R., Jones, E., Kern, R., Larson, E., Carey, C. J., İlhan Polat, Feng, Y., Moore, E. W., VanderPlas, J., Laxalde, D., Perktold, J., Cimrman, R., Henriksen, I., Quintero, E. A., Harris, C. R., Archibald, A. M., Ribeiro, A. H., Pedregosa, F., van Mulbregt, P., Vijaykumar, A., Bardelli, A. P., Rothberg, A., Hilboll, A., Kloeckner, A., Scopatz, A., Lee, A., Rokem, A., Woods, C. N., Fulton, C., Masson, C., Häggström, C., Fitzgerald, C., Nicholson, D. A., Hagen, D. R., Pasechnik, D. V., Olivetti, E., Martin, E., Wieser, E., Silva, F., Lenders, F., Wilhelm, F., Young, G., Price, G. A., Ingold, G. L., Allen, G. E., Lee, G. R., Audren, H., Probst, I., Dietrich, J. P., Silterra, J., Webber, J. T., Slavič, J., Nothman, J., Buchner, J., Kulick, J., Schönberger, J. L., de Miranda Cardoso, J. V., Reimer, J., Harrington, J., Rodríguez, J. L. C., Nunez-Iglesias, J., Kuczynski, J., Tritz, K., Thoma, M., Newville, M., Kümmerer, M., Bolingbroke, M., Tartre, M., Pak, M., Smith, N. J., Nowaczyk, N., Shebanov, N., Pavlyk, O., Brodtkorb, P. A., Lee, P., McGibbon, R. T., Feldbauer, R., Lewis, S., Tygier, S., Sievert, S., Vigna, S., Peterson, S., More, S., Pudlik, T., Oshima, T., Pingel, T. J., Robitaille, T. P., Spura, T., Jones, T. R., Cera, T., Leslie, T., Zito, T., Krauss, T., Upadhyay, U., Halchenko, Y. O. and Vázquez-Baeza, Y. (2020). Scipy 1.0: fundamental algorithms for scientific computing in python, *Nature Methods* **17**.

Visioni, D. and Robock, A. (2022). Future geoengineering scenarios: Balancing policy relevance and scientific significance, *Bulletin of the American Meteorological Society* **103**: E817–E820.
URL: *https://journals.ametsoc.org/view/journals/bams/103/3/BAMS-D-21-0201.1.xml*

Zender, C. S. (2008). Analysis of self-describing gridded geoscience data with netcdf operators (nco), *Environmental Modelling and Software* **23**.

Supporting information for "Identifying the regional emergence of climate patterns in a simulation of stratospheric aerosol injection"

Zachary M. Labe[1,2,*], **Elizabeth A. Barnes**[1], **and James W. Hurrell**[1]

[1] Department of Atmospheric Science, Colorado State University, Fort Collins, CO, USA

[2] Now at Princeton University/NOAA Geophysical Fluid Dynamics Laboratory, Princeton, NJ, USA

[*] Email: zachary.labe@noaa.gov

Submitted to: *Environ. Res. Lett.*

Contents of this file:

Section S1. Text S1-S3:

Text S1: CESM2(WACCM6)

The CESM2(WACCM6) is a fully coupled global climate model and uses an ocean model component derived from the Parallel Ocean Program version 2 (POP2; Smith et al., 2010; Danabasoglu et al., 2012) and a land model component from the Community Land Model version 5 (CLM5; Lawrence et al., 2019). WACCM6 uses 70 vertical levels with a model top reaching $\sim$140 km and includes an internally generated quasi-biennial oscillation, interactive atmospheric chemistry, and improvements to physical parameterizations and gravity wave schemes. This version of CESM2(WACCM6) was also a contribution to the latest Coupled Model Intercomparison Project Phase 6 (Eyring et al., 2016). Although the equilibirum climate sensitivity in CESM2(WACCM6) is substantially higher than its previous model version, it generally scores well in its representation of large-scale climate variability (Meehl et al., 2020; Simpson et al., 2020).

Text S2: Logistic Regression

While the logistic regression model is linear (no hidden layers), aside from the softmax activition function, a number of parameter choices still need to be determined. Specifically, each logistic regression model here uses a categorical cross-entropy loss function and a stochastic gradient descent optimizer (Ruder, 2016) with Nesterov momentum equal to 0.9 (Nesterov, 1983). The learning rate is set to 0.001, and the batch size is set to 32.

To avoid overfitting on the training data, we consider two techniques. First, we use early stopping, which ends the training process if there is no improvement in the validation loss for 10 consecutive epochs and thereafter returns the epoch with the logistic regression model's best weights. Second, we apply ridge regularization (L_2) (Friedman, 2012), which helps to reduce spatial autocorrelation in the climate fields by penalizing larger outlier weights across each input map (Sippel et al., 2019; Barnes et al., 2020). Given that the skill of the logistic regression model may vary depending on the L_2 parameter for each climate variable and geographic region, we explore the sensitivity of the results to a range of possible L_2's for temperature and precipitation in figures S3 and S4, respectively. We then pick a unique L_2 for each region of temperature and precipitation by selecting the L_2 parameter with the highest median accuracy score of validation data across 20 logistic regression models constructed from different combinations of training, testing, and validation ensemble members and random initialization seeds. The final L_2 parameters selected for the logistic regression model results are described in table S1.

Text S3: Artificial Neural Network

For the ANN regression task, we use an architecture of two hidden layers with 10 nodes each. To compare the sensitivity of the prediction results to others ANN architectures, we compare the Spearman's rank correlation on the validation data using a shallower architecture with only one hidden layer and five nodes (figures S5 to S6). As in the earlier predict the year studies using ANNs (e.g., Barnes et al., 2019), we find this metric better captures the importance of the order of the number of years since SCI initiation. Similar to the logistic regression models, we also train the ANNs using a range of L_2 parameters, random initialization seeds, and combinations of training, testing, and validation data. Overall, we find higher median correlations for temperature in all regions using the more complex ANN. This result is also consistent with other architectures we considered, such as using a one layer ANN with 10 nodes or a two layer ANN with five nodes each (not shown). While the dependence of skill on the more complex machine learning approach is not as clear for precipitation, this may be due to the greater influence of internal variability and the subsequent poor prediction skill.

We again use 7 SAI ensemble members for training, 2 ensemble members for validation, and 1 ensemble member as testing for the presentation of the main results. The robustness of these results to the L_2 parameter and combinations of training data are shown in figures S7 and S8 for our final ANN architecture selected in each region. Specifically, we train all the ANNs using a loss function defined by the mean absolute error (MAE) and apply the rectified linear unit (ReLU; Agarap, 2018) activation function in the hidden layers for the nonlinear transformation. The Adam optimizer method (Kingma and Ba, 2014) is used to minimize the loss, the learning rate is set to 0.001, and the batch size is 32. Similar to the logistic regression model, we apply the same early stopping method and select a L_2 parameter unique to each region for temperature and precipitation (table S2), both of which help to limit overfitting on the training data. A detailed introduction to neural networks can be found in Goodfellow et al. (2016), with more specific examples for the atmospheric sciences in Chase et al. (2022).

Section S2. Tables S1-S2:

Table S1. Choice of ridge regularization (L_2) parameter for the final logistic regression (logistic regression) model selected for each region using temperature and precipitation. The sensitivity of the results to this selection are shown in figures S3 to S4.

	Globe	N. Hemisphere	S. Hemisphere	Arctic	Antarctic	Tropics	Southeast Asia	Central Africa	Amazon
temperature	0.5	0.25	0.75	0.1	0.01	0.01	0.01	0.1	0.01
precipitation	0.25	1	0.5	0.75	0.25	0.1	0.1	0.1	0.01

Table S2. Choice of ridge regularization (L_2) parameter for the final artificial neural network (ANN) model selected for each region using temperature and precipitation. The ANN architecture for each region has two hidden layers with 10 nodes each. The sensitivity of the results to this selection are shown in figures S7 to S8.

	Globe	N. Hemisphere	S. Hemisphere	Arctic	Antarctic	Tropics	Southeast Asia	Central Africa	Amazon
temperature	5	1.5	5	1.5	10	1	0.5	5	0.1
precipitation	1	10	1	2	5	5	10	10	1.5

Section S3. Figures S1-S17:

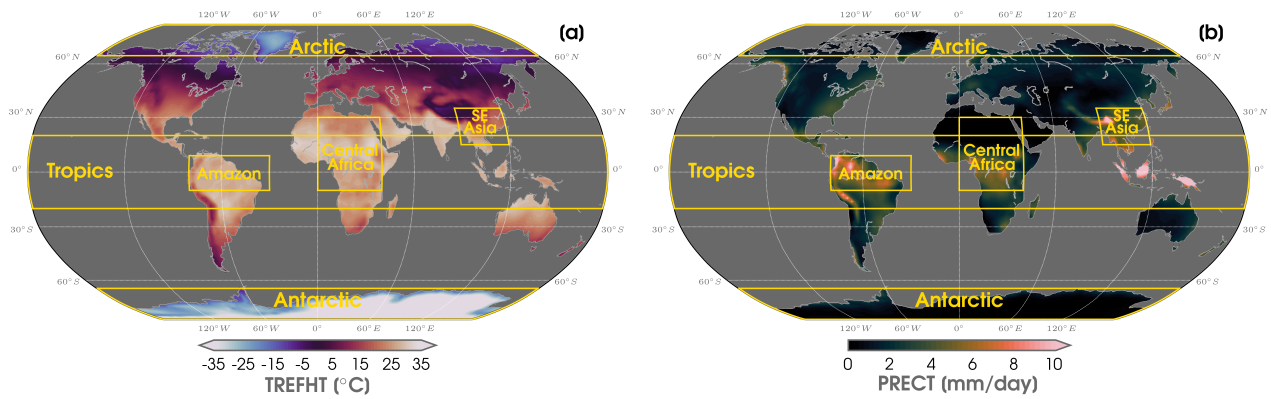

Figure S1. (a) Ensemble mean of annual mean near-surface air temperature (TREFHT) over 2045 to 2069 in ARISE-SAI-1.5. The gold boxes outline the subregions of analysis, including: the Arctic (65°N-90°N and 180°W-180°E), Antarctic (65°S-90°S and 180°W-180°E), Tropics (20°S-20°N and 180°W-180°E), Southeast Asia (15°N-35°N and 90°E-120°E), Central Africa (10°S-30°N and 0°E-40°E), and Amazon (10°S-9°N and 80°W-30°W). (b) As in (a), but for total precipitation (PRECT).

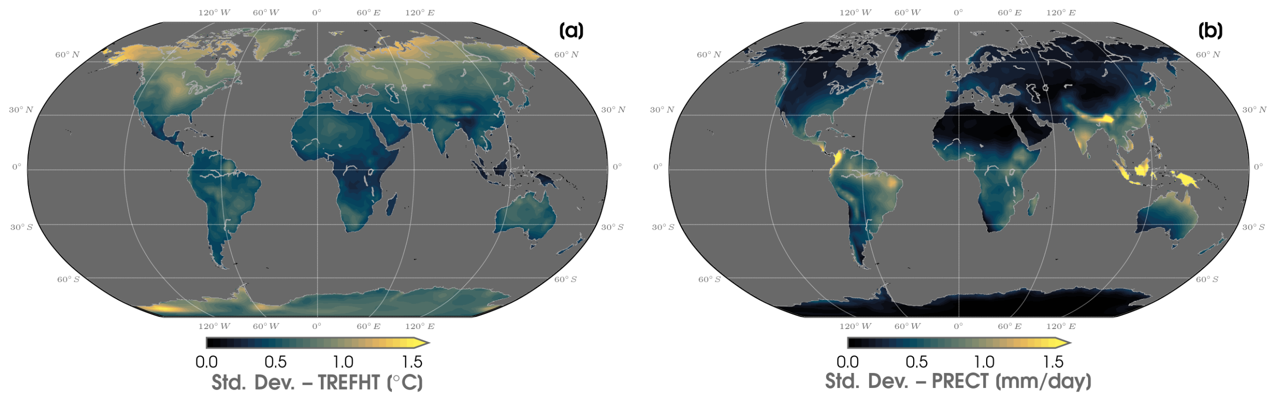

Figure S2. (a) Ensemble mean standard deviation (std. dev.) of annual mean temperature in ARISE-SAI-1.5 computed over 2045 to 2069. The fields of temperature are first linearly detrended at every grid point over the period. The interannual variability is then calculated separately for each ensemble member before taking the ensemble average. (b) As in (a), but for precipitation.

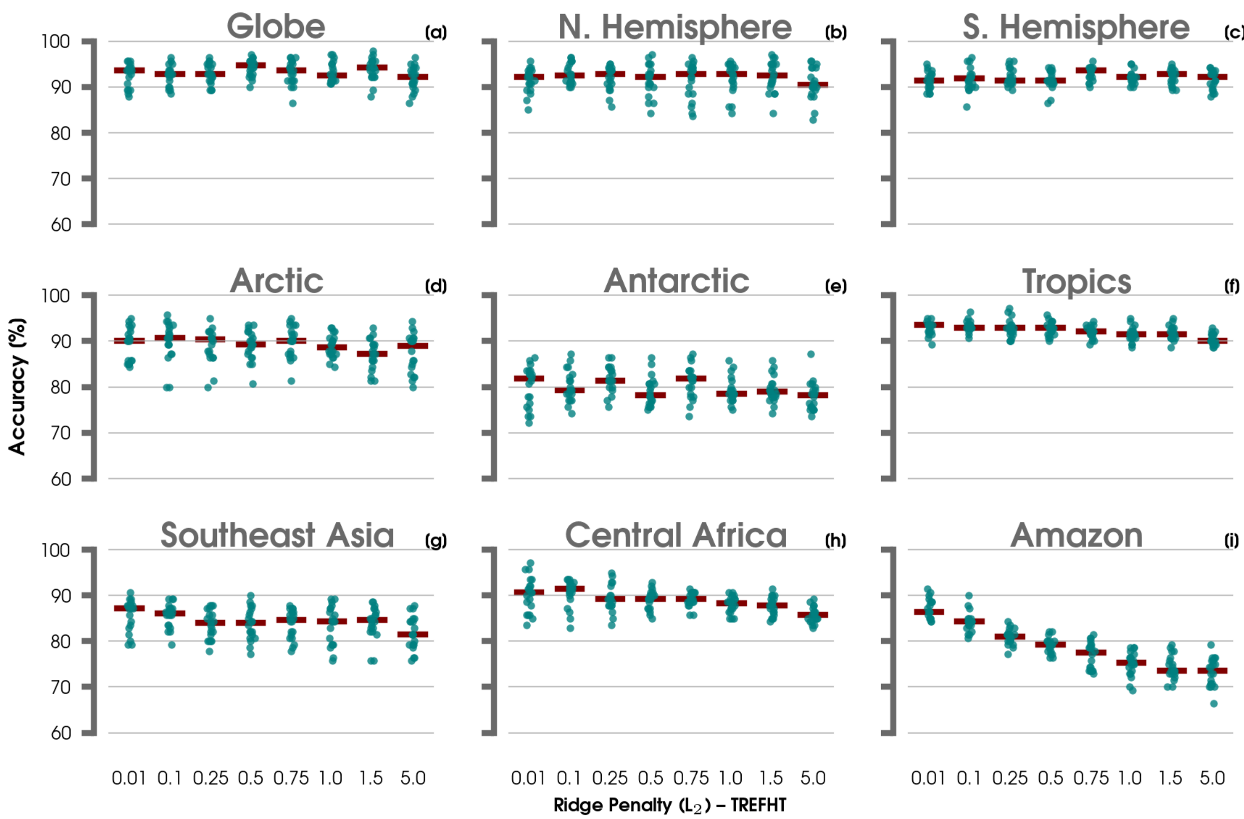

Figure S3. (a) Points showing the total accuracy of validation data (ensemble members) for the logistic regression model with inputs of global maps of temperature for different L_2 regularization values (0.01, 0.1, 0.25, 0.5, 0.75, 1.0, 1.5, 5.0). Each set of points are comprised of 20 logistic regression model iterations (different combinations of training, testing, and validation ensemble members and random initialization seeds), and the median score is shown with a red horizontal line. (b-i) As in (a), but for logistic regression models with inputs of land areas in the Northern Hemisphere, Southern Hemisphere, Arctic, Antarctic, Tropics, Southeast Asia, Central Africa, and Amazon.

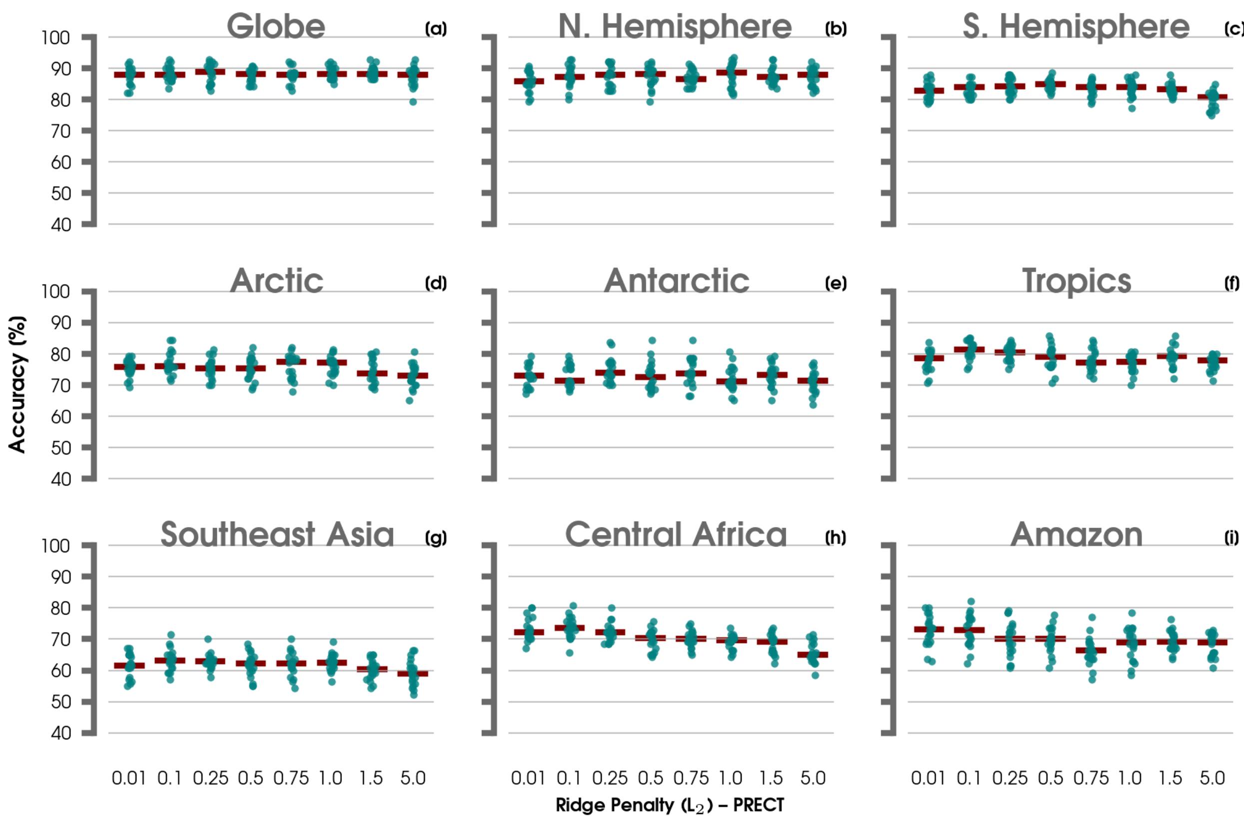

Figure S4. As in Figure S3, but for inputs of precipitation.

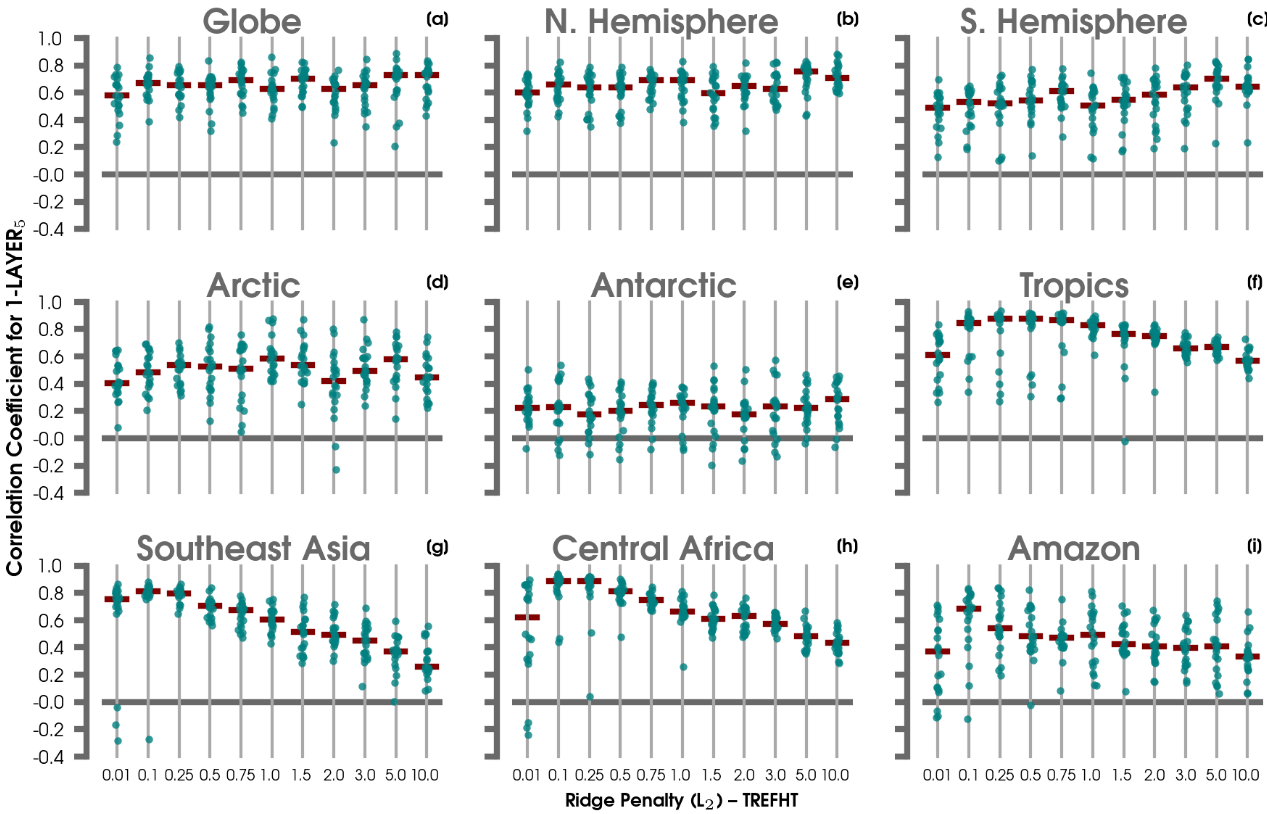

Figure S5. (a) Points showing the Spearman correlation coefficient of validation data (ensemble members) for an ANN model with 1 hidden layer of 5 nodes using inputs of global maps of temperature and different L_2 regularization values (0.01, 0.1, 0.25, 0.5, 0.75, 1.0, 1.5, 2.0, 3.0, 5.0, 10). Each set of points are comprised of 20 ANN iterations (different combinations of training, testing, and validation ensemble members and random initialization seeds), and the median score is shown with a red horizontal line. (b-i) As in (a), but for an ANN with inputs of land areas in the Northern Hemisphere, Southern Hemisphere, Arctic, Antarctic, Tropics, Southeast Asia, Central Africa, and Amazon.

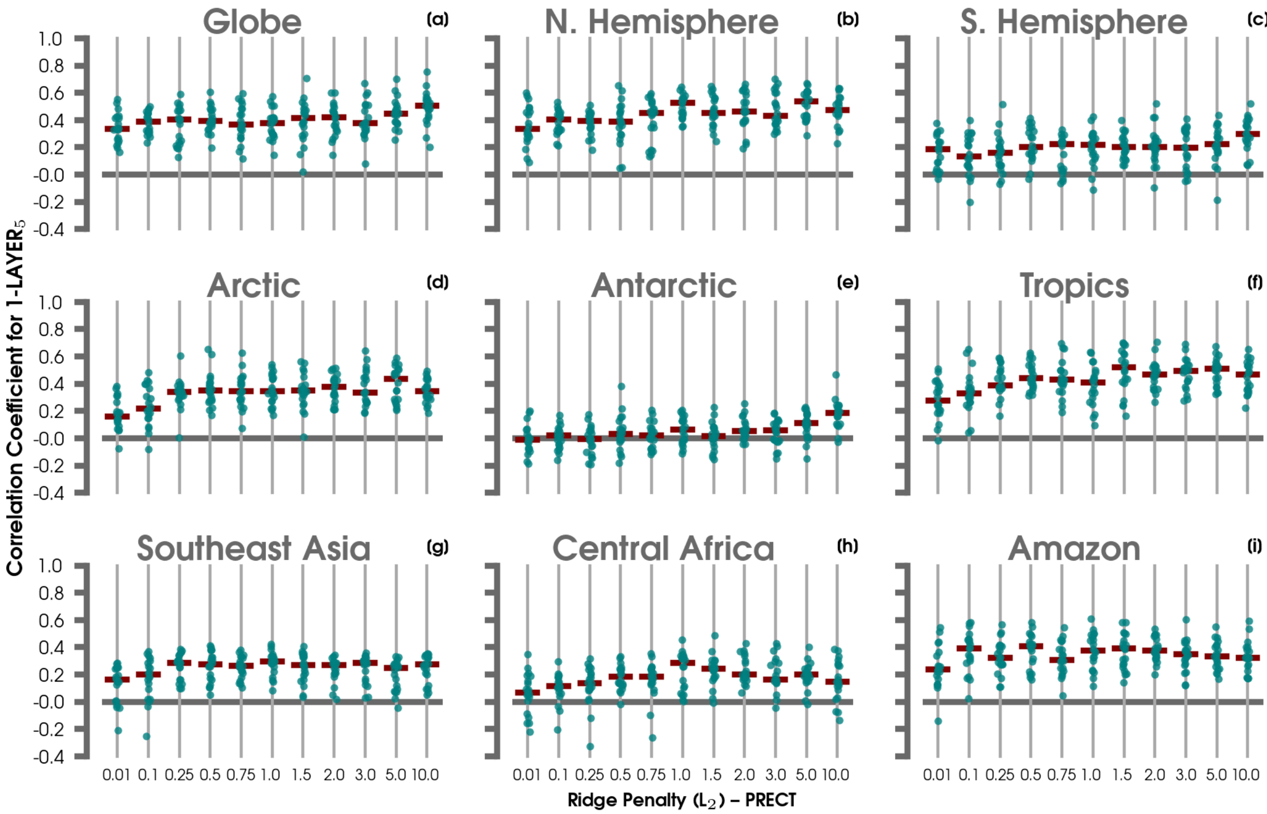

Figure S6. As in Figure S5, but for inputs of precipitation maps.

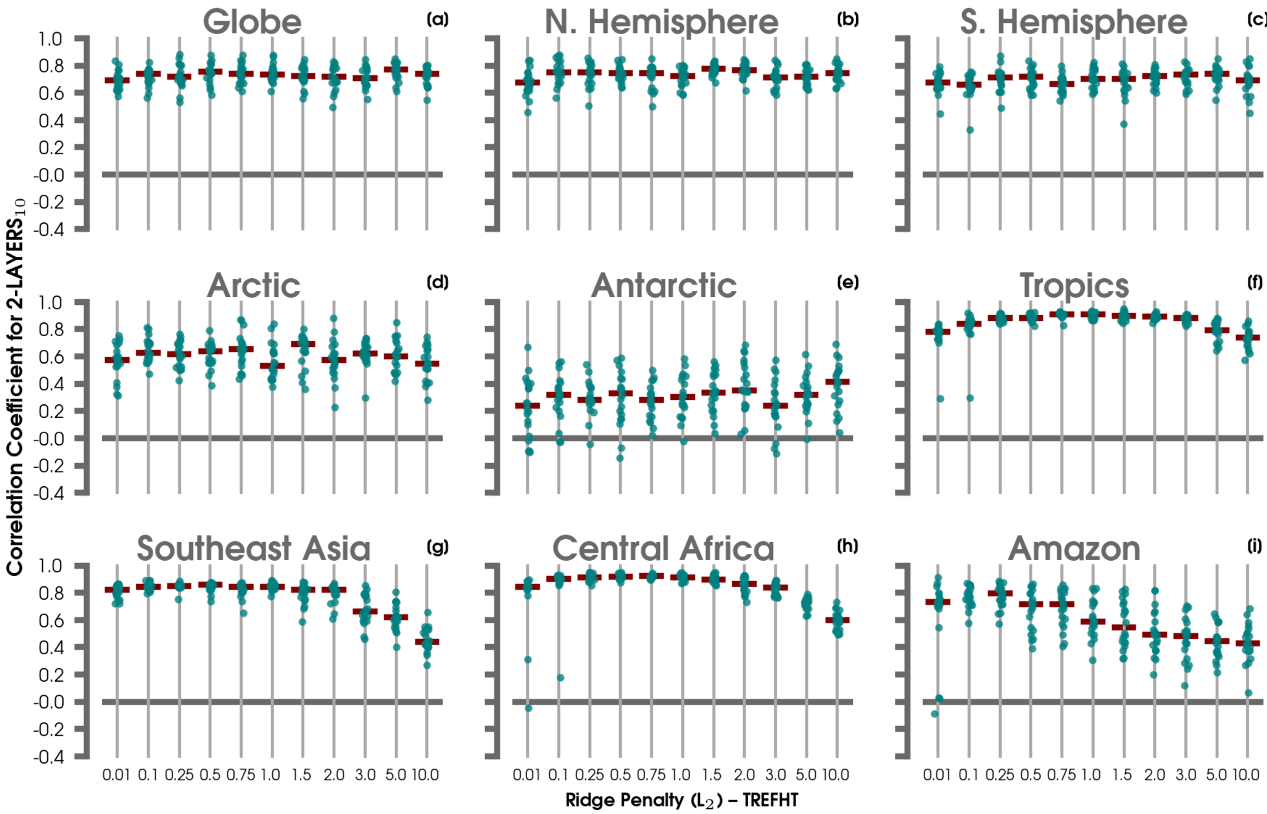

Figure S7. As in Figure S5, but using an ANN with 2 hidden layers of 10 nodes each.

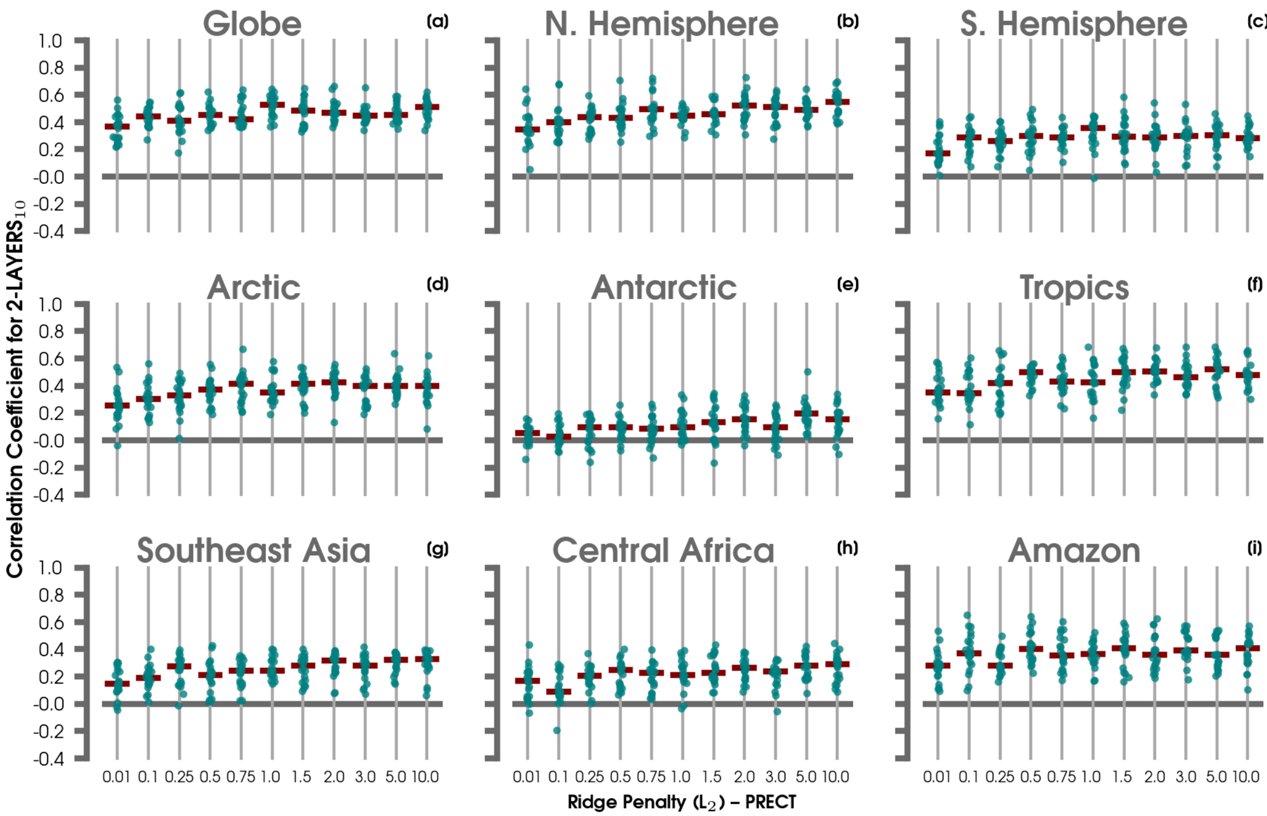

Figure S8. As in Figure S6, but using an ANN with 2 hidden layers of 10 nodes each.

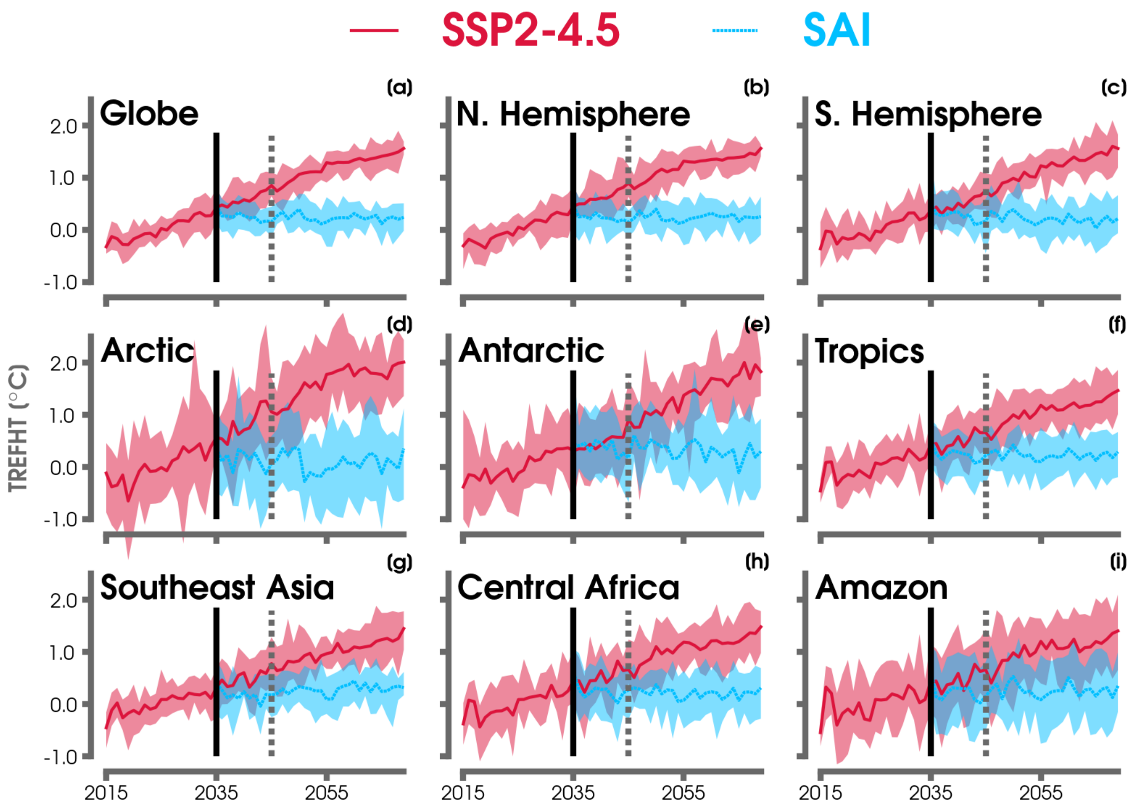

Figure S9. (a) Annual mean time series of global temperature anomalies over land areas for the ensemble mean in SSP2-4.5 (solid red line) and SAI (dashed blue line). The ensemble spread is shown with the color shading. A black vertical line denotes the deployment of SAI in the year 2035 for the ARISE-SAI-1.5 simulation. The gray dashed vertical line separates the two time periods of analysis: 2035-2044 and 2045-2069. Anomalies are computed from a common reference period of 2015 to 2034 in the SSP2-4.5 simulation. (b-i) As in (a), but for land areas in the Northern Hemisphere, the Southern Hemisphere, the Arctic, the Antarctic, the Tropics, Southeast Asia, Central Africa, and the Amazon

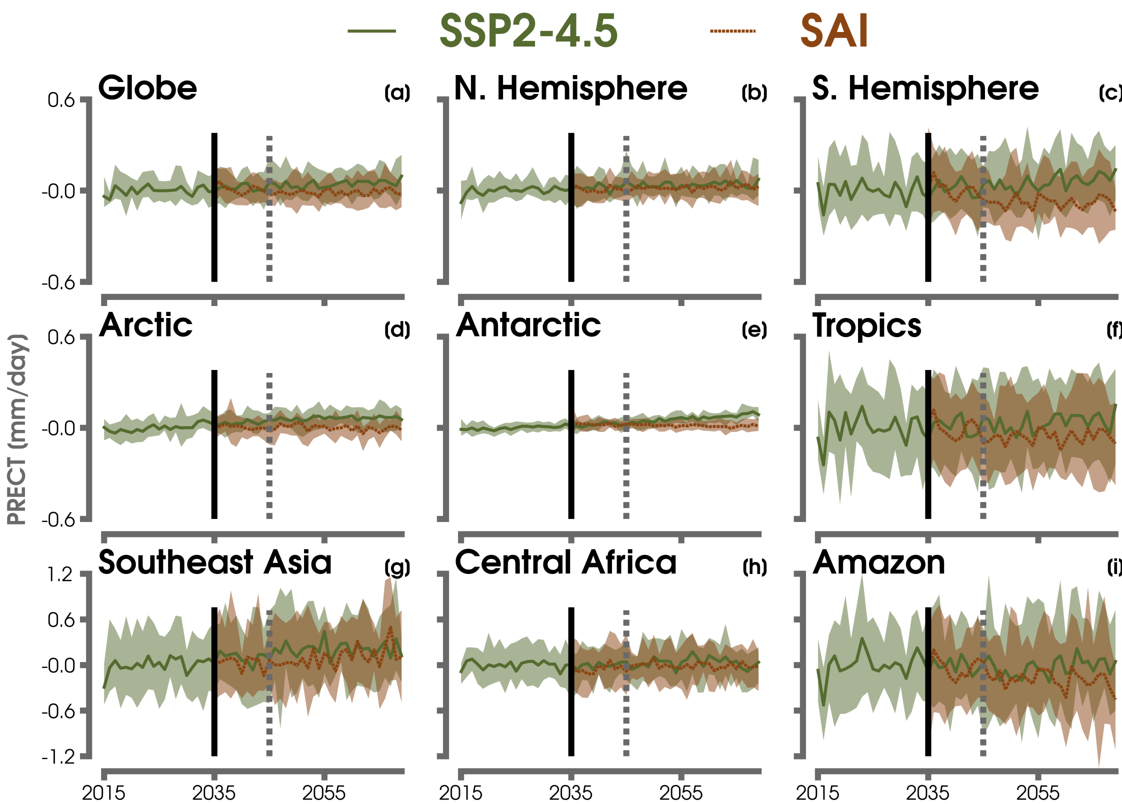

Figure S10. As in Figure S9, but for average precipitation in SSP2-4.5 (solid green line) and SAI (dashed brown line).

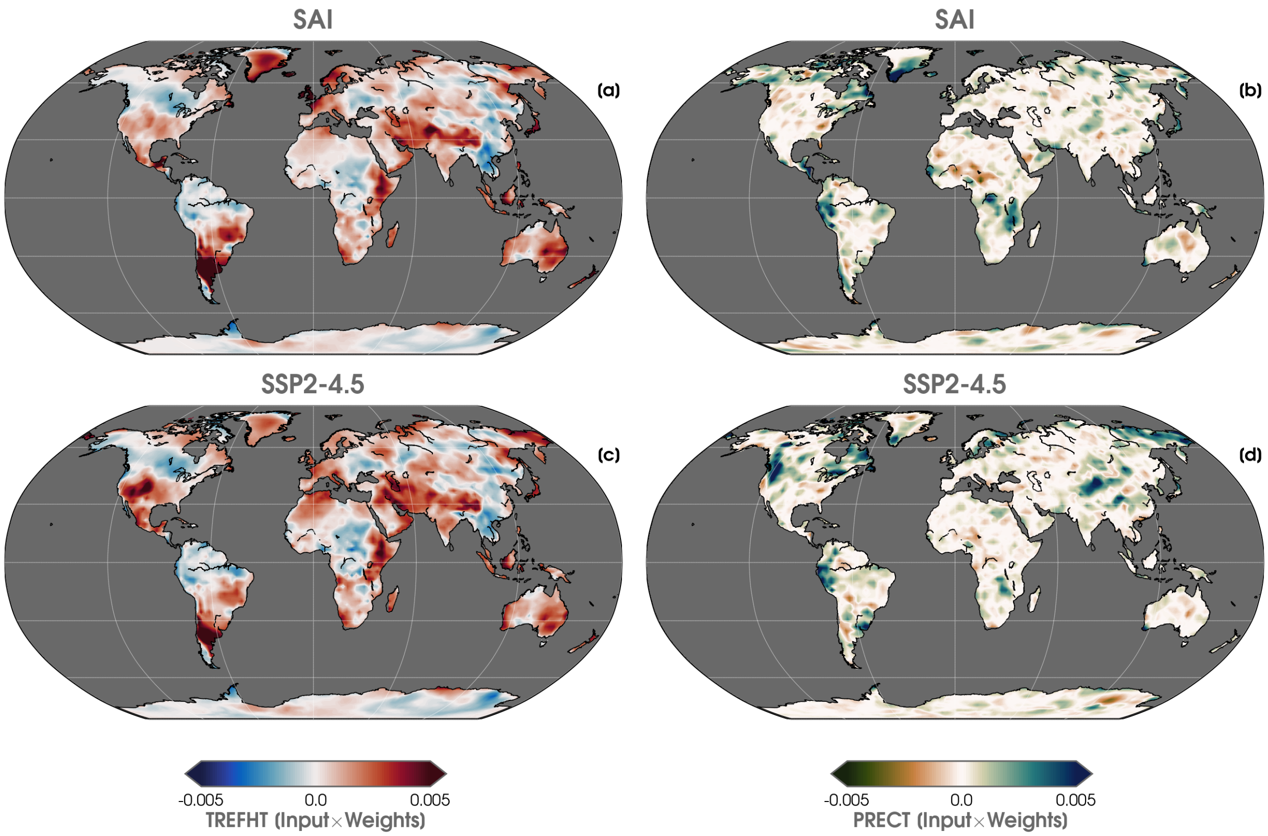

Figure S11. (a) Contribution map (input*weights) for the correct logistic regression predictions of temperature averaged over 2035 to 2069 using SAI testing data. (b) As in (a), but for the SAI predictions of precipitation. (c) As in (a), but for the SSP2-4.5 predictions of temperature. (d) As in (a), but for the SSP2-4.5 predictions of precipitation. Positive contributions in each maps can be interpreted as regions that drive the logistic regression model to its respective prediction.

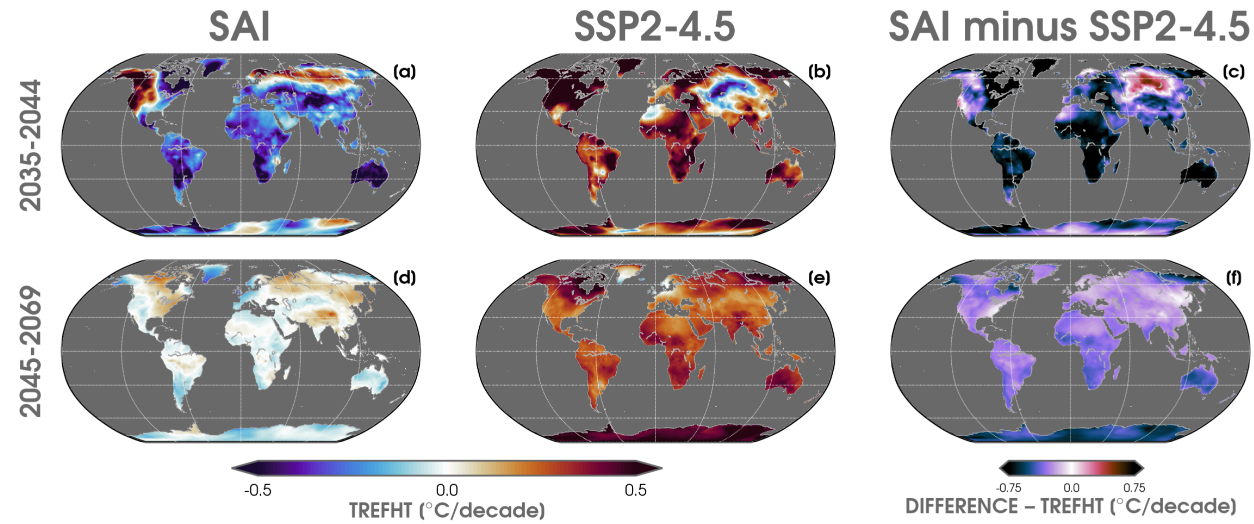

Figure S12. Annual linear least squares trends of temperature (°C per decade) over 2035-2044 (a, b) and 2045-2069 (d, e) for the ensemble means of SAI (a, d) and SSP2-4.5 (b, e). The difference in decadal temperature trends from SAI minus SSP2-4.5 is shown for 2035-2044 (c) and 2045-2069 (f).

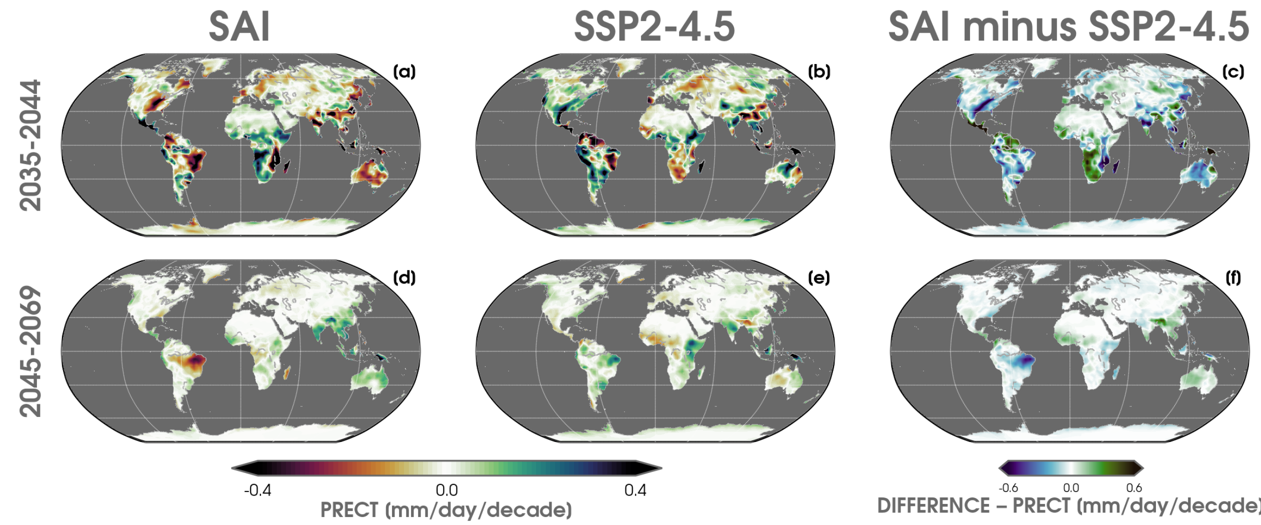

Figure S13. As in Figure S12, but for precipitation trends.

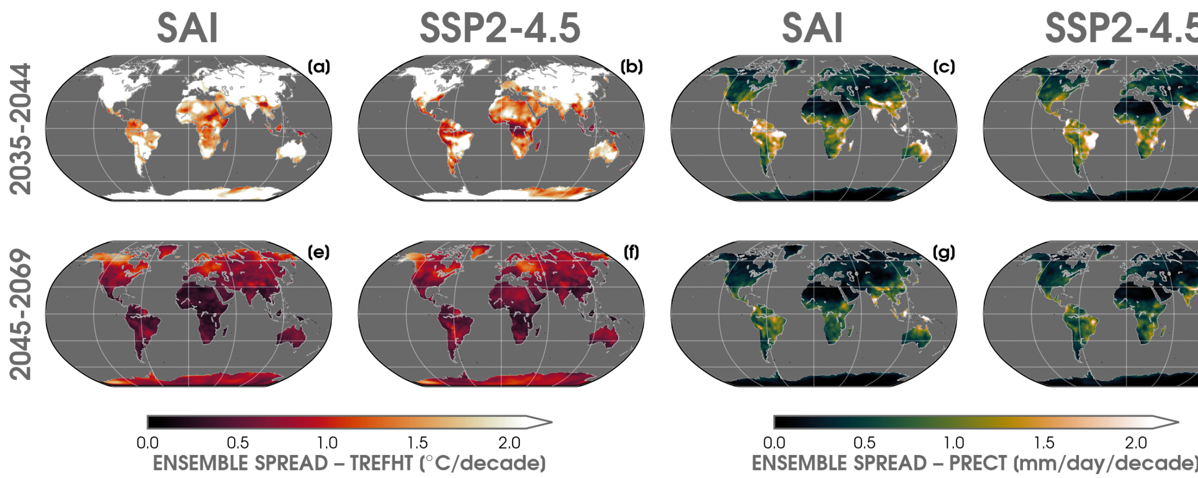

Figure S14. The ensemble spread of temperature trends (°C per decade) over 2035-2044 (a, b) and 2045-2069 (e,f) for the SAI (a, e) and SSP2-4.5 (b, f) simulations, and the ensemble spread of precipitation trends (°C per decade) over 2035-2044 (c, d) and 2045-2069 (g,h) for the SAI (c,g) and SSP2-4.5 (d,h) simulations.

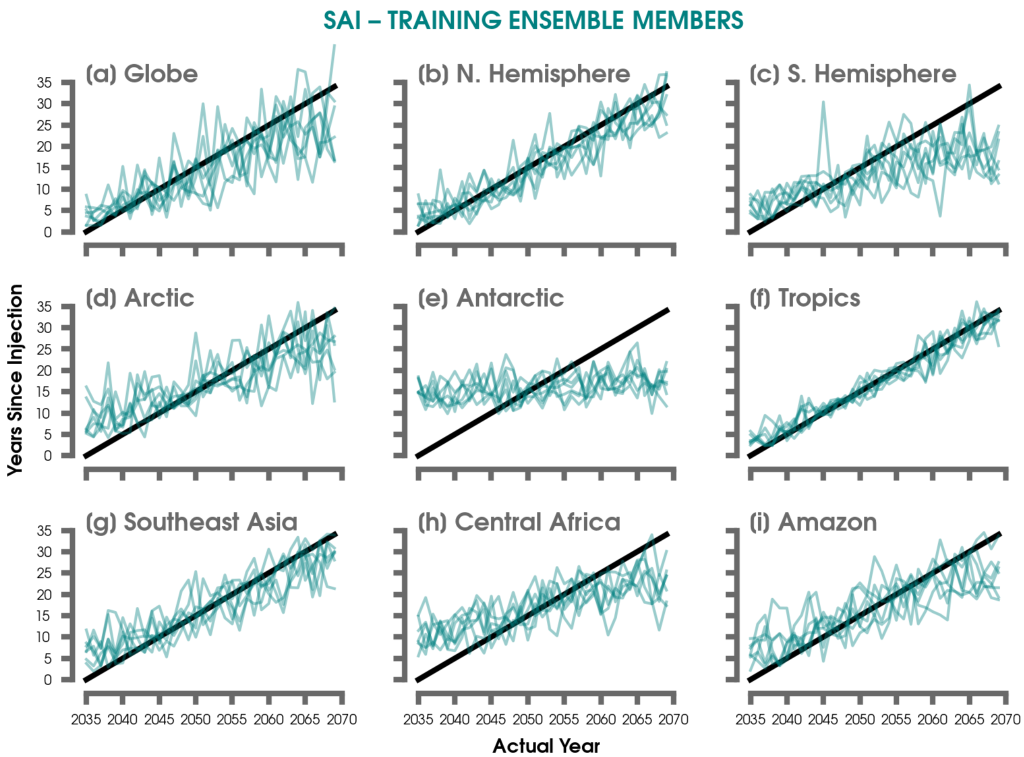

Figure S15. Predictions of the number of years since SAI injection by the ANN for the 7 SAI training ensemble members for (a) global land maps, (b) the Northern Hemisphere, (c) the Southern Hemisphere, (d) the Arctic, (e) the Antarctic, (f) the Tropics, (g) Southeast Asia, (h) Central Africa, (i) and the Amazon. The 1:1 lines (or perfect predictions) are shown in black.

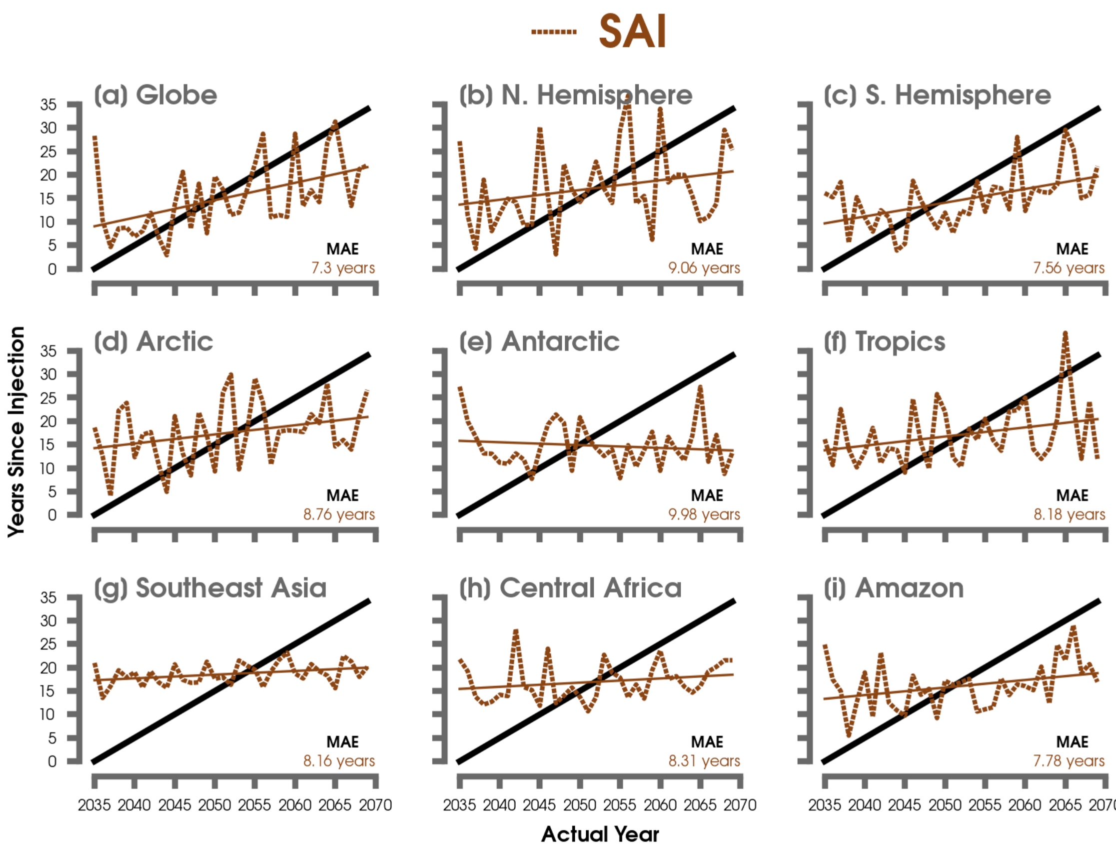

Figure S16. Predictions of the number of years since SAI injection by the ANN for the single SAI testing ensemble member of precipitation for (a) global maps, (b) the Northern Hemisphere, (c) the Southern Hemisphere, (d) the Arctic, (e) the Antarctic, (f) the Tropics, (g) Southeast Asia, (h) Central Africa, (i) and the Amazon. The mean absolute error (MAE) for each region is included in the lower right-hand corner. The brown solid lines shows the linear least squares fit through the predictions of each regional ANN. The 1:1 lines (or perfect predictions) are shown in black.

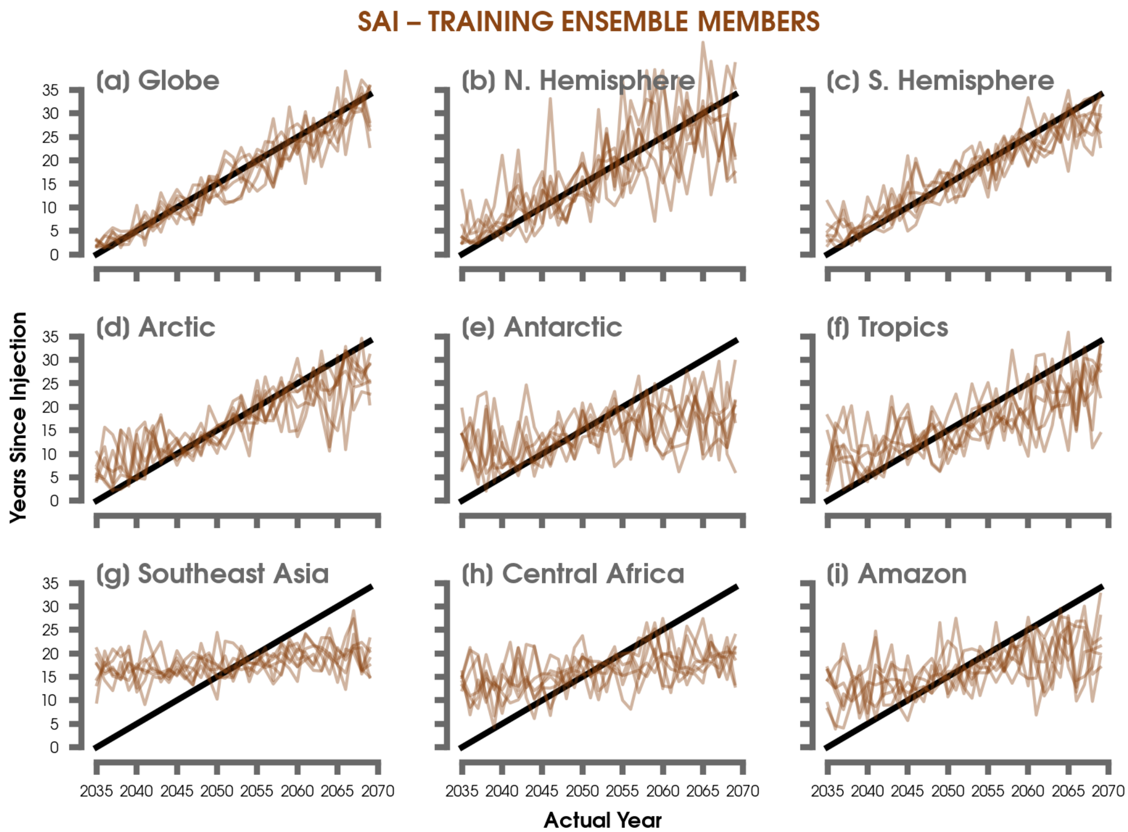

Figure S17. As in Figure S15, but for precipitation.

Section S4. References:

Agarap, A. F. (2018). Deep learning using rectified linear units (relu), *arXiv* .
URL: *http://arxiv.org/abs/1803.08375*

Barnes, E. A., Hurrell, J. W., Ebert-Uphoff, I., Anderson, C. and Anderson, D. (2019). Viewing forced climate patterns through an ai lens, *Geophysical Research Letters* **46**: 13389–13398.
URL: *https://onlinelibrary.wiley.com/doi/abs/10.1029/2019GL084944*

Barnes, E. A., Toms, B., Hurrell, J. W., Ebert-Uphoff, I., Anderson, C. and Anderson, D. (2020). Indicator patterns of forced change learned by an artificial neural network, *Journal of Advances in Modeling Earth Systems* **12**.
URL: *https://onlinelibrary.wiley.com/doi/10.1029/2020MS002195*

Chase, R. J., Harrison, D. R., Lackmann, G. and McGovern, A. (2022). A machine learning tutorial for operational meteorology, part ii: Neural networks and deep learning, *arXiv* .
URL: *https://arxiv.org/abs/2211.00147v1*

Danabasoglu, G., Bates, S. C., Briegleb, B. P., Jayne, S. R., Jochum, M., Large, W. G., Peacock, S. and Yeager, S. G. (2012). The ccsm4 ocean component, *Journal of Climate* **25**.

Eyring, V., Bony, S., Meehl, G. A., Senior, C. A., Stevens, B., Stouffer, R. J. and Taylor, K. E. (2016). Overview of the coupled model intercomparison project phase 6 (cmip6) experimental design and organization, *Geoscientific Model Development* **9**: 1937–1958.

Friedman, J. H. (2012). Fast sparse regression and classification, *International Journal of Forecasting* **28**: 722–738.

Goodfellow, I., Bengio, Y. and Courville, A. (2016). *Deep Learning*.

Kingma, D. P. and Ba, J. L. (2014). Adam: A method for stochastic optimization, *3rd International Conference on Learning Representations, ICLR 2015 - Conference Track Proceedings* .
URL: *https://arxiv.org/abs/1412.6980v9*

Lawrence, D. M., Fisher, R. A., Koven, C. D., Oleson, K. W., Swenson, S. C., Bonan, G., Collier, N., Ghimire, B., van Kampenhout, L., Kennedy, D., Kluzek, E., Lawrence, P. J., Li, F., Li, H., Lombardozzi, D., Riley, W. J., Sacks, W. J., Shi, M., Vertenstein, M., Wieder, W. R., Xu, C., Ali, A. A., Badger, A. M., Bisht, G., van den Broeke, M., Brunke, M. A., Burns, S. P., Buzan, J., Clark, M., Craig, A., Dahlin, K., Drewniak, B., Fisher, J. B., Flanner, M., Fox, A. M., Gentine, P., Hoffman, F., Keppel-Aleks, G., Knox, R., Kumar, S., Lenaerts, J., Leung, L. R., Lipscomb, W. H., Lu, Y., Pandey, A., Pelletier, J. D., Perket, J., Randerson, J. T., Ricciuto, D. M., Sanderson, B. M., Slater, A., Subin, Z. M., Tang, J., Thomas, R. Q., Martin, M. V. and Zeng, X. (2019). The community land model version 5: Description of new features, benchmarking, and impact of forcing uncertainty, *Journal of Advances in Modeling Earth Systems* **11**: 4245–4287.
URL: *https://onlinelibrary.wiley.com/doi/full/10.1029/2018MS001583*

Meehl, G. A., Arblaster, J. M., Bates, S., Richter, J. H., Tebaldi, C., Gettelman, A., Medeiros, B., Bacmeister, J., DeRepentigny, P., Rosenbloom, N., Shields, C., Hu, A., Teng, H., Mills, M. J. and Strand, G. (2020). Characteristics of future warmer base states in cesm2, *Earth and Space Science* **7**: e2020EA001296.
URL: *https://agupubs.onlinelibrary.wiley.com/doi/10.1029/2020EA001296*

Nesterov, Y. (1983). A method for unconstrained convex minimization problem with the rate of convergence o(1/k2), *Doklady AN USSR* **269**.

Ruder, S. (2016). An overview of gradient descent optimization algorithms, *arXiv* .
URL: *http://arxiv.org/abs/1609.04747*

Simpson, I. R., Bacmeister, J., Neale, R. B., Hannay, C., Gettelman, A., Garcia, R. R., Lauritzen, P. H., Marsh, D. R., Mills, M. J., Medeiros, B. and Richter, J. H. (2020). An evaluation of the large-scale atmospheric circulation and its variability in cesm2 and other cmip models, *Journal of Geophysical Research: Atmospheres* **125**: e2020JD032835.
URL: *https://onlinelibrary.wiley.com/doi/full/10.1029/2020JD032835*

Sippel, S., Meinshausen, N., Merrifield, A., Lehner, F., Pendergrass, A. G., Fischer, E. and Knutti, R. (2019). Uncovering the forced climate response from a single ensemble member using statistical learning, *Journal of Climate* **32**.

Smith, R., Jones, P., Briegleb, B., Bryan, F., Danabasoglu, G., Dennis, J., Dukowicz, J., Eden, C., Fox-Kemper, B., Gent, P., Hecht, M., Jayne, S., Jochum, M., Large, W., Lindsay, K., Maltrud, M., Norton, N., Peacock, S., Vertenstein, M. and Yeager, S. (2010). The parallel ocean program (pop) reference manual: Ocean component of the community climate system model (ccsm), *Rep. LAUR-01853* **141**.